universität wien

DIPLOMARBEIT / DIPLOMA THESIS

Titel der Diplomarbeit / Title of the Diploma Thesis

„Impacts of surface and thermal treatments on the performance of Cu_2ZnSnS_4 (CZTS) thin films photovoltaic device“

verfasst von / submitted by

Quynh Nhu Nguyen, BSc

angestrebter akademischer Grad / in partial fulfilment of the requirements for the degree of

Diplom-Ingenieurin (Dipl.-Ing.)

Wien, 2021 / Vienna, 2021

Studienkennzahl lt. Studienblatt / degree programme code as it appears on the student record sheet:	UA 066 658
Studienrichtung lt. Studienblatt / degree programme as it appears on the student record sheet:	Masterstudium Chemie und Technologie der Materialien UG2002
Betreut von / Supervisor:	Univ.-Prof. Dr. Eleonora Hendrika Gertruda Mezger-Backus

Acknowledgements

I would like to express my gratitude to my supervisors Dr. Rachmat Adhi Wibowo, Dr. Theodoros Dimopoulos, Univ.-Prof. Dr. Ellen Backus and Anies Mutiari for providing guidance, feedback and emotional support throughout this project.

List of Abbreviations

PV	Photovoltaic
SCR	Space Charge Region
CZTS	Cu_2ZnSnS_4
CZTSe	$Cu_2ZnSnSe_4$
UPW	Ultrapure water
RT	Room temperature
AZO	Aluminium doped Zinc Oxide
i-ZnO	intrinsic Zinc Oxide
ITO	Indium Tin Oxide
DC	Direct Current
QE	Quantum Efficiency
IQE	Internal Quantum Efficiency
EQE	External Quantum Efficiency
SP	Spectral Responsitivity
I-V	Current-Voltage
FF	Fill Factor
SEM	Scanning Electron Microscope
BSE	Back-scattered Electron
SE	Secondary Electron
J_{SC}	Short Circuit Current
V_{OC}	Open Circuit Voltage
XRD	X-Ray Diffraction

Contents

Abstract

Kësterit $Cu_2ZnSn(S,Se)_4$ (CZT(S,Se)) Dünnschichtmaterialien als Absorberschicht in Solarzellen zählen zu den vielversprechenden neuen Photovoltaiktechnologien. Dass sie vollständig aus nicht-toxischen Elementen bestehen, die im Überschuss in der Erdkruste vorhanden sind und zusätzlich äußerst kosteneffizient in der Produktion sind, und dennoch einen Wirkungsgrad von deutlich über 10 % erreichen, zählt zu ihren wesentlichsten Vorteilen.

Diese Diplomarbeit ist ein kooperatives Projekt, welches von der Österreichische Forschungsförderungsgesellschaft (FFG) unterstützt, und zwischen dem Austrian Institute of Technology (AIT) und der Universität Wien durchgeführt wurde.

Das Ziel dieser Diplomarbeit ist es, CZT(S,Se)-Solarzellen mittels einer Lösung in der sich die Vorläuferelemente Cu, Zn, Sn und Chalkogene wie Schwefel und Selen befinden, herzustellen. Die Synthese von einer derartigen Kësterit CZT(S,Se) Hochleistungssolarzelle trifft auf die Herausforderung, dass sich beim Kristallisationsprozess Sekundärphasen aus Zn-reichen und Cu-armen Umgebungen aufgrund einer Nicht-stöchiometrie bilden können, welche die photovoltaischen Eigenschaften der Solarzellen negativ beeinflussen können. Der Herstellungsprozess der CZT(S,Se)-Absorberschichten wird aufgrund dessen modifiziert und optimiert, indem diese Sekundärphasen mittels Rasterelektronenmikroskop, Röntgenbeugung und Raman Spektroskopie identifiziert und anschließend durch chemisches Ätzen, wie zum Beispiel mit einer HCl- oder KCN-Lösung, selektiv entfernt werden. Die Auswirkungen des chemischen Ätzens werden anhand von den Reaktionsbedingungen systematisch in Bezug auf Ätzzeit und Konzentration untersucht und optimiert. Die daraus gewonnenen CZT(S,Se)-Absorberschichten werden anschließend in Solarzellen eingebunden und mit modernen Technologien der Photovoltaikmessmethoden charakterisiert um wichtige Informationen aus den Strom-Spannungs-Kurven und des Externen Quantenwirkungsgrades zu erhalten.

Am Ende dieser Arbeit wurde eine CZT(S,Se)-basierte Solarzelle hergestellt, welche nach einem systematischen Optimierungsprozess des chemischen Ätzens einen Wirkungsgrad von 8.3 % aufweisen konnte.

Abstract

$Cu_2ZnSn(S,Se)_4$ (CZT(S,Se)) kesterite thin film absorber materials in solar cells are a key material in the emerging photovoltaic (PV) technologies since they are non-toxic and consist entirely of earth abundant elements, while still reaching an efficiency above 10 %. Due to their abundancy, low-production cost, non-toxicity and efficiency, they are a promising contestant in renewable energy technologies.

This thesis is a cooperative project funded by the Austrian Research Promotion Agency (FFG) and coordinated by the Energy Conversion and Hydrogen Department of the Austrian Institute of Technology (AIT) and the University of Vienna.

The aim of this thesis is to fabricate a CZT(S,Se)-based photovoltaic device in which the CZT(S,Se) thin film absorber layer is prepared using a Cu, Zn, Sn and chalcogenide-based precursor ink. The synthesis of CZT(S,Se) absorbers for high-performing PV devices inaugurate challenges of secondary phase growth in Zn-rich and Cu-poor environment caused by off-stoichiometric conditions. The CZT(S,Se) absorber layer will be therefore modified and optimized by eliminating unwanted secondary phases, such as Cu_2S and/or SnS_2, which degrades the performance of a photovoltaic device. The secondary phases will firstly be identified using structural characterization methods such as scanning electron microscopy and X-Ray diffraction and selectively removed using chemical etchants such as KCN and HCl. The process of chemical etching will be systematically studied and modified to the optimum in concentration and etching time.

The CZT(S,Se) thin film absorber acts as a component of a photovoltaic device which will be studied with state-of-the-art characterization techniques such as current-voltage analysis and quantum efficiency measurement.
To further improve the performance of the PV device, thermal treatment of the PV device on a hot plate will be undergone.

Through a set of deposition, the systematic analysis and optimization of etching parameters and thermal treatment of the CZT(S,Se)-absorber layer, a PV device with a conversion efficiency of 8.3 % was obtained by the end of the study.

1 Theoretical Background

1.1 Photovolatics

Photovoltaics is defined as the process of sunlight conversion into electricity using solar cells. At present, photovoltaic (PV) systems have globally become an established part of the electrical energy technologies as they provide power in an extended range from tenths of watts up to hundreds of megawatts. By the end of 2015, the total global cumulative capacity of installed PV systems exceeded 227 gigawatts, which is equivalent to about 280 coal-fired plants. In 2014, in Germany, Italy and Greece, 6 to 11% of the annual electricity generated originated from PV systems. [1] PV systems were intentionally developed to act as a reliable and durable electricity provider for space applications such as satellites. Due to their low CO_2 emissions PV systems are considered a promising technology to overcome global warming, which is caused by the staggering amount of greenhouse gases.
Therefore, the implementation of solar cells nowadays is driven by the need to reduce the emission of greenhouse gases:

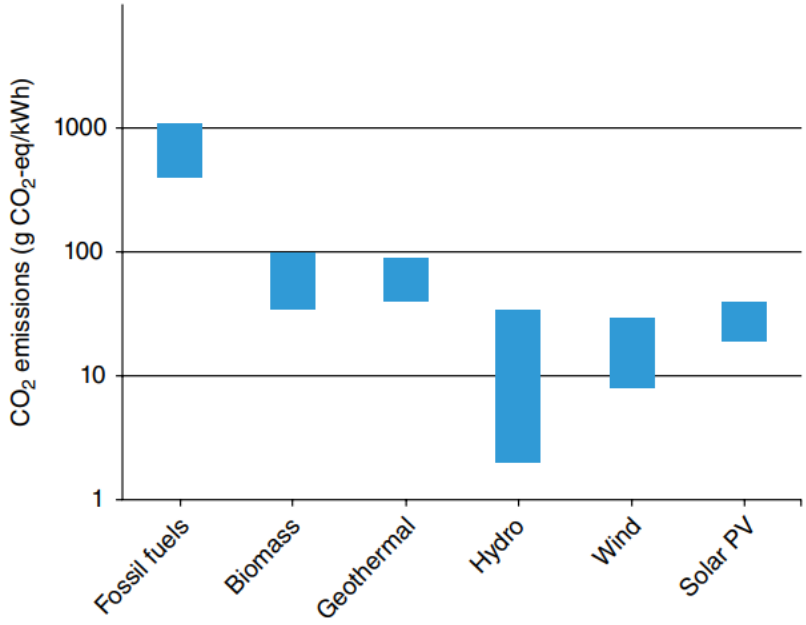

Figure 1: Various energy technologies in comparison regarding their CO_2 emissions. Figure is taken from [2].

If one compares PV systems to other energy technologies in Figure 1, especially to power plants, which are based on fossil fuels, such as coal, the difference in CO_2 emissions per kWh of generated electricity is remarkable: coal-based power plants emit as much as 800 g CO_2/kWh while PV systems stay as low as 30 g CO_2/kWh. To overcome global warming, the implementation of PV systems as renewable energy technologies, together with wind energy and hydro-power, become indispensable. One can therefore expect a further implementation of PV systems in off-grid applications. [2]

1.1.1 Photoelectric Effect

A photon can be characterised either by a wavelength λ or equivalently an energy E. The inverse relationship between the energy of a photon and the wavelength of the light is given by the following equation

$$E = \frac{hc}{\lambda} \tag{1}$$

h ... Planck's constant $[6.626 \cdot 10^{-34} joule \cdot s]$
c ... Speed of Light $[2.998 \cdot 10^{8} m \cdot s^{-1}]$
λ ... Wavelength [nm]

The phenomenon that the energy of a photon can elevate an electron from the valence band into the conduction band is also known as the photoelectric effect. This phenomenon is widely observed in metals as the conduction band and the valence band overlap: electromagnetic radiation in ultraviolet (UV) range hits the metal surface and electrons are subsequently ejected. The ejected electrons are also known as photoelectrons.
In order for the photoelectric effect to occur in semiconductors, the energy of the photon needs to be larger than the material's band gap to elevate the electron from the valence band into the conduction band. Therefore, the photoelectric effect is the conversion of photons having an energy larger than the material's band gap into electricity. [3] [4]

1.1.2 Semiconductor materials in Photovoltaics

The principle of conductors, semiconductors and insulators can be described with the band theory which is presented in Figure 2. The bands represent all permitted energy states for an electron: the highest state occupied by valence electrons is called valence band whereas the lowest unoccupied band is also known as the conduction band. The forbidden zone between valence band and conductor band is also known as band gap E_g, which is the difference of the lowest energy level of the conductor band E_C and the highest energy level of the valence band E_V. An electron needs to overcome the band gap in order to be excited from the valence band into the conductor band. These electrons then become conductor electrons and contribute to the conductivity of a material. At absolute zero T=0 K the valence electrons remain strongly bound, no electrical current can be obtained as there are no available charge carriers. By increasing the temperatures the electrons start to loosen their bonds and start to move. If the temperature is high enough the electrons retain enough energy to overcome the band gap. The size of the band gap determines whether a material classifies as an insulator, a semiconductor or a metal: while the band gap in metals is virtually non-existing as the valence band and conductor band overlap, the band gap in insulator materials are usually greater than 3 eV, meaning that the electrons cannot overcome the band gap to enter the conductor band, not even at high temperatures. Diamond, as a well-known insulator, has a band gap of E_g=7.3 eV. A semiconductor typically has a band gap which is smaller than 3 eV, which allows the valence bands to be elevated into the conductor band at medium temperatures. Otherwise semiconductors act as insulating materials at low temperatures. A noteworthy semiconductor material is Silicon with a band gap of 1.12 eV. [5]
Semiconductors have a broad range of band gaps, which, depending on the condition, can either act an insulator

or as a conductor. Since this change in electronic properties can be controlled by voltage, electric field, doping, light and temperature, semiconductor materials find numerous applications in electronics. [2]

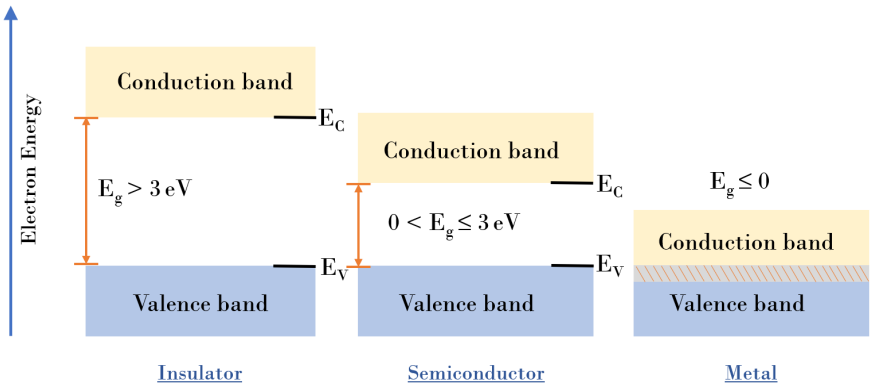

Figure 2: Energy band diagrams of an insulator, a semiconductor and a metal.

On the grounds that semiconductors have poor electrical properties, one can reach for doping as a technique to vary the number of free charge carriers, such as electrons and electron holes to the desired conductivity: Conventional photovoltaics are well represented with doped Silicon, a semiconductor crystal with single covalent bonds and 4 valence electrons. The dopants, e.g. Boron with 3 valence electrons or Phosphorus with 5 valence electrons are integrated into the crystal lattice. When Silicon is doped with Phosphorus one can speak of n-doping as four valence electrons in the lattice enter a bond with the neighboring atom but the fifth valence electrons finds no open bonds and can therefore act as a free charge carrier. In n-doped materials electrons act as the majority carriers and holes as the minority carriers. In this case, the Phosphorus acts as a donor atom. n-doping creates a new energy level in the band diagram below the conductor band shown on the left hand side in Figure 3.

Contrary to phosphorus, in p-doped materials the dopant Boron induces the opposite effect: Boron, having 3 valence electrons, can attract an outer electron, thus leaving a hole in the valence band of silicon atoms. Therefore, Boron acts as an acceptor atom. In p-type doped materials the holes become the majority charge carrier and electrons the minority charge carriers. Analogously to n-type doping, a new energy level, the acceptor level, in the band diagram appears right above the valence band. [5]

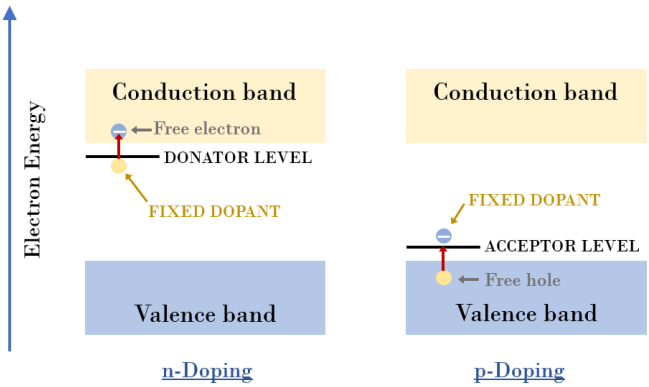

Figure 3: Band model of doped n-type and p-type semiconductors.

1.1.3 Working Principle of a Solar Cell

The working principle of a solar cell is based on two main effects: the photoelectric effect and the charge carrier separation. Due to the photoelectric effect, a photon transfers its kinetic energy onto an electron, which is then excited from the valence band into the conduction band. This action can only be guaranteed given that the energy of the photon E_{Photon} is larger than the band gap E_g. This process leaves behind an electron hole in the valence band, resulting in an electron-hole pair, also known as exciton.

In order to generate electrical current, the electron, once excited to the conduction band, needs to be collected and driven through an external load.

The carrier separation is obtained through an electric field in a pn-junction, which is a junction between a p- and n-doped semiconducting material. In p-doped materials, holes act as majority carriers and electrons are minority carriers. In a n-doped materials, electrons are majority carriers while holes are minority carriers. When p-type and n-type semiconductors are in contact, forming a pn-junction, a carrier diffusion flux is obtained due to a carrier concentration gradient. The diffusion flux causes a static electric field at the junction, which is called the Space Charge Region (SCR), also known as depletion region, which acts as the charge carrier separator. If an external circuit is provided connecting the two sides of the pn-junction, electrons can flow through a load and an electrical power can be used. [5] [6]

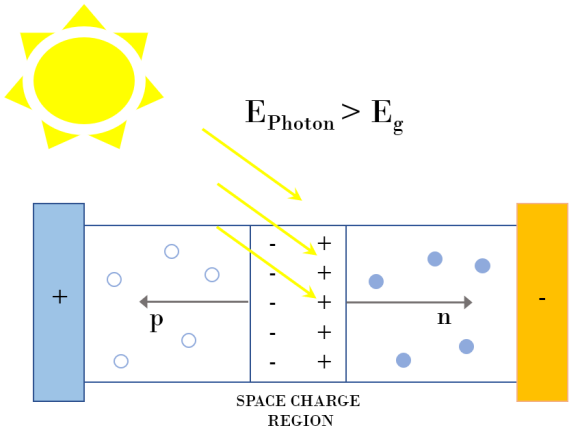

Figure 4: Principle of p-n junction in a solar cell and charge transport phenomena.

The performance of the solar cell is measured by the efficiency of solar conversion into electricity, or photon to current efficiency. The explanation and calculation to determine the solar cell efficiency is described in the Experimental section of this thesis.

1.2 CZT(S,Se) as Photovoltaics

$Cu_2ZnSn(S,Se)_4$ (CZT(S,Se)) thin films as an alternative absorber material for photovoltaic devices belong to the emerging solar cell technologies. Current conventional thin film PV technologies rely on CdTe and $Cu(In,Ga)Se_2$ (CIGS) as absorber compounds. CdTe and CIGS achieve efficiency values greater than 20 %. However, the incorporation of rare Telluride and Indium and the toxicity of Cadmium are a huge disadvantage of their utilization in the long run as photovoltaics are nowadays developed to be in favour of the environment. Therefore, CZT(S,Se), as a non-toxic compound, which solely consists of earth abundant elements, is a promising competitor in the field of PV technology. [7] Even though the highest recorded PV efficiency of a kesterite CZTS device, which was 12.6 % in 2019 [8], it may not defeat CIGS regarding the PV efficiency, but CZT(S,Se) photovoltaics beat CIGS in terms of cost efficiency, non-toxicity and component availability.

Due to the ability of covering a broad range of band gaps depending on the ratio of Se/S, CZT(S,Se)s can be applied in a variety of technological fields such as solar cells, counter electrode material in a photoelectrochemical cell and photo catalysis. [9]

The solar cell structure of CZT(S,Se)-based PV devices is adapted from the related chalcopyrite CIGS, with a Molybdenum back contact, a CdS buffer layer and a ZnO and Aluninium-doped Zinc Oxide (AZO) layer on top as state-of-the-art.

CZTS has a high absorption coefficient that suits very well with multiple layer-based structures when used as absorption layer for PV devices. CZTS has a band gap of 1.4-1.5 eV which is very close to the band gap required by the common semiconducting photovoltaics of 1.50 eV. [10]

The band gap of the CZTS can be modified and optimized for maximum solar radiation absorption by incorporating Selenium. By controlling the S/(S+Se) ratios the band gap of CZT(S,Se) thin films can vary from 1.0 eV in pure CZTSe to 1.5 eV in pure CZTS. [11]

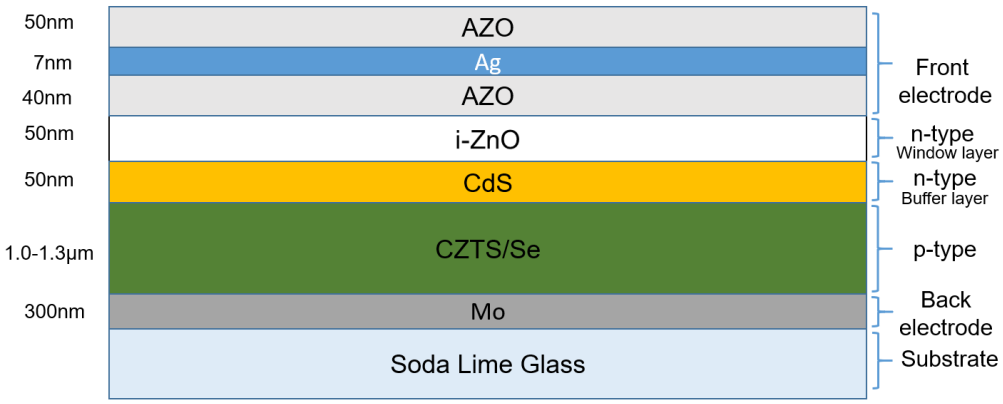

Figure 5: Schematic structure of the cross-section of a photovoltaic device with p-type material CZT(S,Se) absorber. CdS acts as n-type buffer layer and intrinsic ZnO as a n-type window layer. Mo acts as a back electrode and the front electrode consists of a sandwich layer of AZO and Ag.

The structure of the PV device that was prepared, modified and characterized in this thesis is shown in Figure 5. The CZT(S,Se) is deposited on Mo-coated soda lime glass, which functions as the back contact. Mo is a common

used electrode material for optical applications, since it has a high optical reflectivity and the electric conductivity as the metal work function of Mo is equal to 5 eV.

The CZT(S,Se) is the p-type material which acts as the absorber layer of the PV device. In general, for absorber layers, a p-type material with an optimum value of band gap and high absorption coefficient is desired, since these kind of materials lead to a high efficiency in solar cell technologies.

The CdS acts as a n-type buffer layer, which in this case reduces strain and defects in the absorber layer. CdS has a band gap of 2.4 eV which enables the photons in the UV range of the solar radiation to be transmitted to the absorber layer. Buffer layers provide a band gap alignment between the absorber layer and the window layer, which in this device is the intrinsic Zinc Oxide (i-ZnO). ZnO is a transparent conducting oxide with a band gap of 3.3 eV. It therefore does not absorb any visible light. [12]

The photovoltaic device is completed with a sandwich layer of Aluminium-doped ZnO (AZO) and Ag used as the front contact to collect the electrons and to distribute to the external load. The electrode AZO/Ag/AZO has been used in PV devices as a standard material at AIT.

1.2.1 Chemical Etching

The challenge of preparing CZT(S,Se) materials is the CZT(S,Se) extremely narrow single phase existence zone in the phase diagram at 400 °C, as marked as "*" in Figure 6. [13] Therefore, as a consequence, when the CZT(S,Se) materials exhibit off-stoichiometric compositions it can result in secondary phases like as $Cu_2Sn(S,Se)_3$, Zn(S,Se), Cu_2(S,Se) and Sn(S,Se). These secondary phases appear on the kesterite CZT(S,Se) surface as well as in the bulk and they can potentially degrade the performance of photovoltaic devices. [14]
If the secondary phase has a lower band gap than the actual absorber, Cu_2S has a band gap equal to 1.2 eV whereas CZTS has a band gap of 1.5 eV, it will limit the open circuit voltage (V_{OC}) of the solar cell. [9]

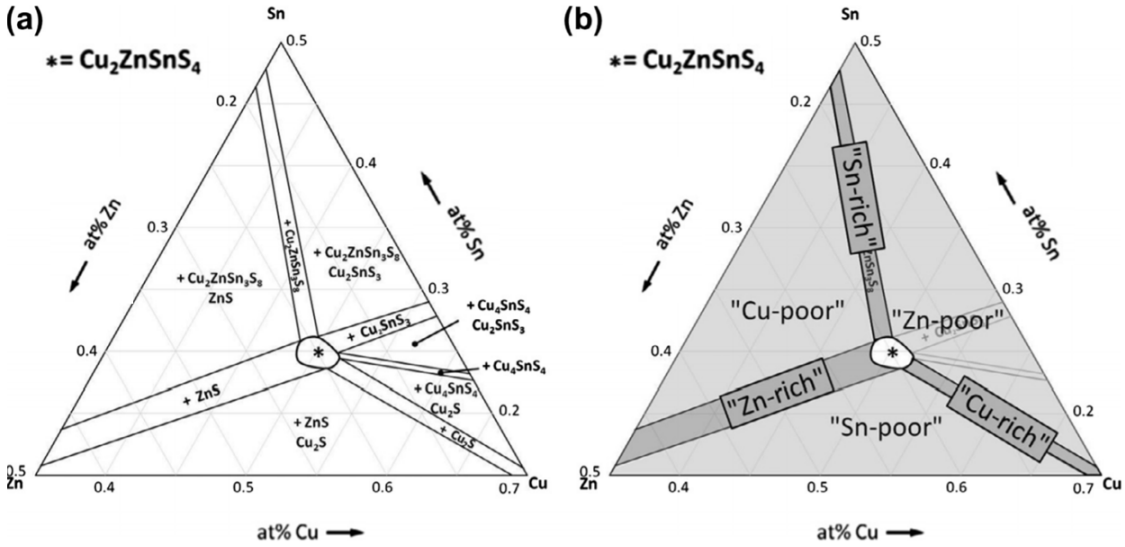

Figure 6: a) Ternary phase diagram of CZTS at 400°C including the expected secondary phases, (b) ternary CZTS phase diagram including regions in which secondary phases should be expected to form at that composition. This figure is taken from [13].

Chemical etching has been a helpful tool in the processing of solar cells, since the secondary phases can be removed selectively: Cu-rich phases such as $Cu_x(S,Se)_y$ can be removed with 10 % w/w KCN at room temperature (RT) and Zn-rich phases dissolve in 5-10 % v/v HCl at 75 °C. [15]

$$2\,\mathrm{Cu(S,Se)} + 5\,\mathrm{KCN} + 2\,\mathrm{KOH} \longrightarrow 2\,\mathrm{KCu(CN)_2} + 2\,\mathrm{K_2(S,Se)} + \mathrm{KCNO} + \mathrm{H_2O} \quad (1)$$

$$2\,\mathrm{HCl} + \mathrm{ZnS} \longrightarrow \mathrm{ZnCl_2} + \mathrm{H_2S} \quad (2)$$

Since in literature HCl as an acid is a commonly used etching agent and in other literature, the oxidising agent H_2O_2 can be found [16], it was suggested that HNO_3 could be a promising etching agent since it is both, an acid and an oxidising agent. The reaction mechanism is suggested as followes:

$$\mathrm{Cu_2S} + 14\,\mathrm{HNO_3} \longrightarrow 2\,\mathrm{Cu(NO_3)_2} + \mathrm{H_2SO_4} + 10\,\mathrm{NO_2} + 6\,\mathrm{H_2O} \quad (3)$$

1.2.2 Thermal Treatment of PV Device

The thermal treatment of a CZTS PV device has been proven to contribute to its PV performance: Studies have found that photovoltaic performance parameters such as open circuit voltage (V_{OC}), short circuit current density (J_{SC}), fill factor (FF) and efficiency of CZTS solar cells were improved for a PV device which was incorporated with an Indium Tin Oxide (ITO) window layer, after a thermal treatment at 220 °C. In particular, the V_{OC} of the CZTS device could be increased by 57 mV when the window layer was post-annealed at 200 °C. [17]
In addition, thermal treatments at temperatures from 150 to 500 °C have improved the absorber component in terms of surface morphology, crystal structure, transmittance behavior, band gap, and electrical properties. Especially higher temperatures induced the phase changes from wurtzite CZTS to cubic CZTS and then tetragonal CZTS, causing an improvement in the crystallinity degree and electrical properties. [18]

2 Experimental

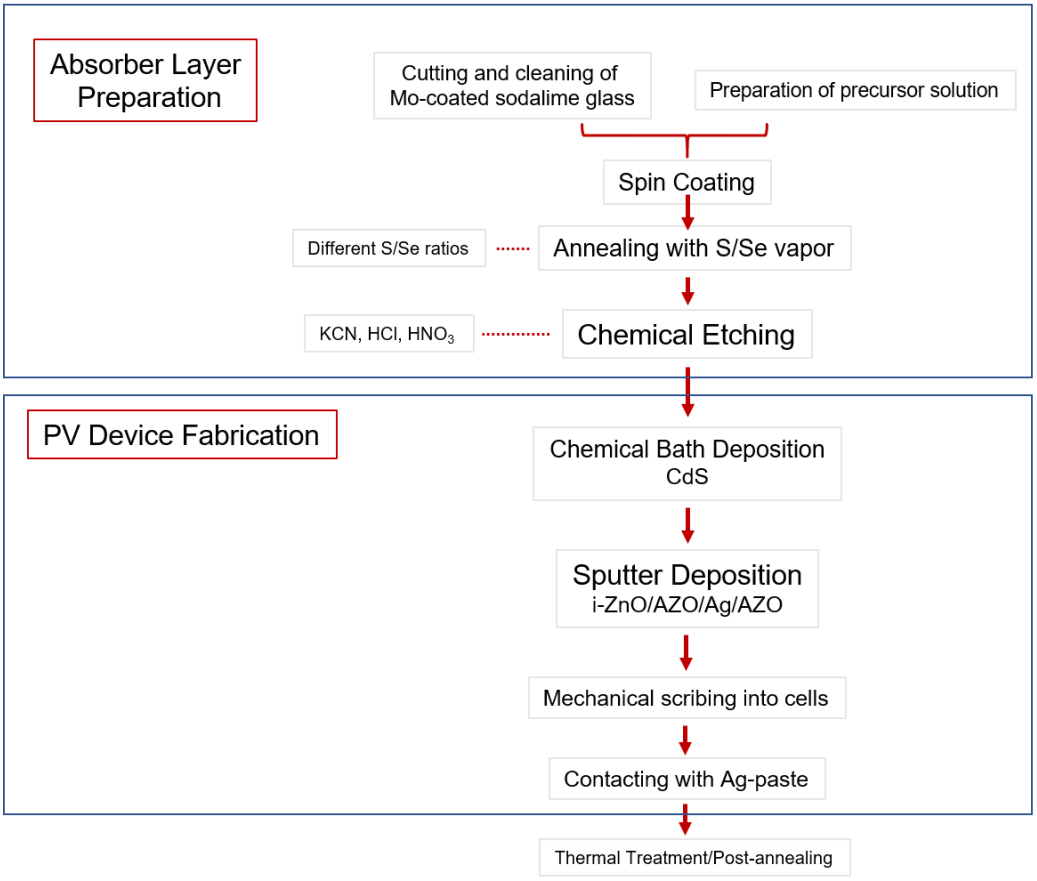

Figure 7: Schematic description of working steps of the fabrication a CZT(S,Se) PV Device in this thesis.

The steps of the overall PV device fabrication are represented in a flowchart in Figure 7. Since this thesis mainly focuses on the optimization of preparation and treatment of the kesterite CZT(S,Se) absorber layer, the overall PV device fabrication is devided in two sections: the fabrication and treatment of the CZT(S,Se) absorber and the depositions of the remaining components of the kesterite CZT(S,Se) photovoltaic device, which incorporate among other procedures the chemical bath deposition of the CdS buffer layer and the sputter deposition of the i-ZnO/AZO/Ag/AZO layer.

2.1 Absorber Layer Preparation

Molybdenum-coated glass was used as a substrate and was cut into 2.4x2.4 cm pieces and firstly cleaned with acetone in the ultrasonic bath for 15 minutes. The substrates were rinsed subsequently in ultrapure water (UPW) and cleaned with isopropanol in the ultrasonic bath for 15 minutes to ensure no organic or any other contamination was left on the substrate. After cleaning, the samples were held in a 2 M NH_4OH solution for 5 minutes, rinsed with ultrapure water and dried with N_2 with the aim to remove all oxide layers on the Mo surface.

For the absorber layer itself, a precursor solution of the CZTS was prepared as followes: for 10 ml of precursor solution 1.4083 g Thiourea (1.85 M), 1.010 g $SnCl_2$ (0.53 M), 0.5316 g $ZnCl_2$ (0.39 M) and 0.7664 g $CuCl_2$ (0.57 M) were dissolved in 10 ml DMSO and stirred for 30 min until a clear solution was obtained.

The solution was deposited on the Mo-coated glass with spin coating at 1500 rpm for 30 seconds. To remove all organic solvent and to densify the precursor layer, the sample was placed on a heating plate with $T_{set} = 300°C$ for 30-60 s. This process of spin-coating and annealing on the hot-plate was repeated nine to twelve times in total.

Figure 8: Setup for spin coating of CZT(S,Se) precursor ink onto Mo-coated soda lime glass substrate.

The crystallisation of the CZTS precursor layer was done by sintering the precursor layer in a quartz tube furnace under sulfur vapor. Two samples were placed in a graphite crucible shown in Figure 9 with 200 mg Sulphur/Selenium.

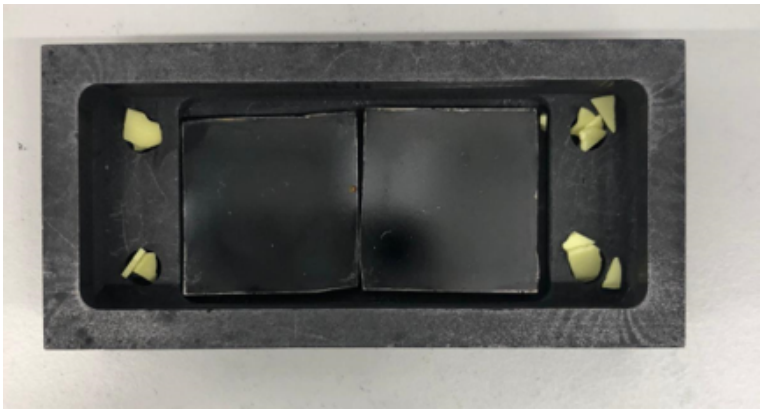

Figure 9: As-deposited CZTS absorber placed in a graphite crucible with 200 mg Sulphur.

The Se/S ratios are listed in Table 1. The ratio Se/S is defined as $x = \frac{m(Se)[g]}{m(S)+m(Se)[g]}$.

Table 1: Preparation of CZTSSe absorber using different ratios of Se and S.

Sample	x	m(S) [mg]	m(Se) [mg]
CZTS	0	200	0
CZTSSe	0.25	150	50
CZTSSe	0.5	100	100
CZTSSe	0.75	50	150
CZTSe	1	0	200

After purging the quartz tube with N_2, the graphite crucible was placed in the tube furnace. The annealing process of the samples took 4 h in total: the furnace was heated with a ramping rate of 10 °C/min for an hour. Once the furnace reached 620 °C, the samples were annealed for 2 h and subsequently cooled for another hour.

2.1.1 Chemical Etching

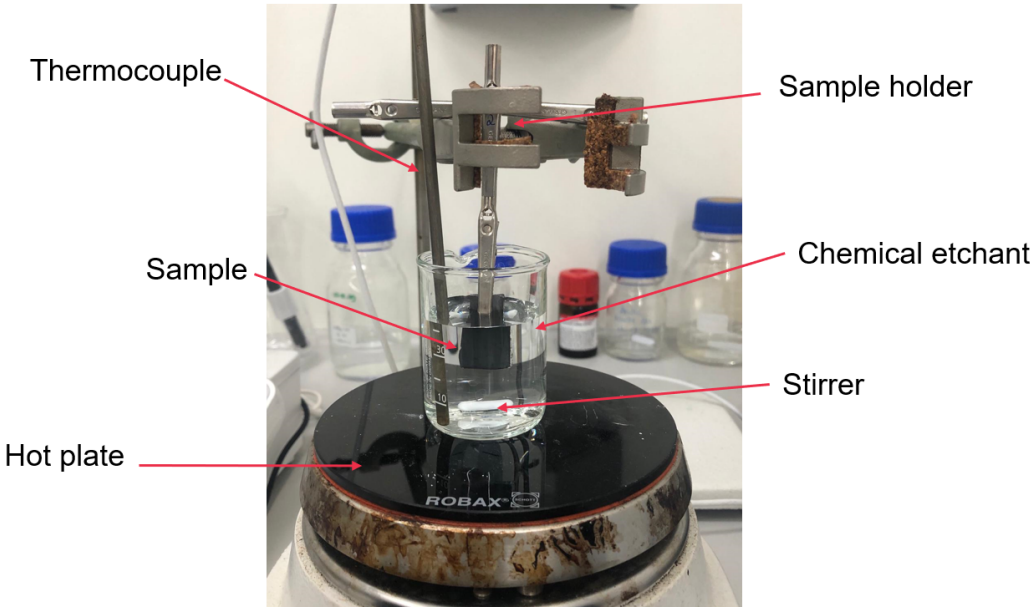

Figure 10: Setup for Chemical Etching of CZT(S,Se) absorber.

The absorber samples were placed in a small beaker with the etchants. During the etching process the solution was stirred. After etching, the samples were rinsed with ultrapure water and dried with N_2.
The etching was first performed on as-annealed CZTS absorber samples with 9 Layers of spin coated precursor ink using 10 % KCN and 10 % HCl in order to observe any effects on the CZTS absorber, which will be later on characterized using Scanning electron microscopy (SEM), X-Ray diffraction (XRD) and Raman spectroscopy.

In further experiments, the etched CZTSSe absorbers were incorporated in photovoltaic devices and characterized using a solar simulator and EQE measurement to determine the photovoltaic efficiency. Additionally other etching parameters such as concentration and etching time as well HNO_3 as an additional etchant was introduced and executed on photovoltaic devices with CZTSSe with a Se/S ratio of x=0.25, and 12 Layers of Spin coating, absorber material as shown in Table 2.
According to the results of these experiments, further investigations on the effects of the KCN etching were enacted, which are shown in Table 3.

Table 2: Different etchants

	Etchant	Concentration	Time	Temperature
1	None (Reference)	-	-	-
2	HCl	5% v/v	30s	75°C
3	HCl	5% v/v	60s	75°C
4	KCN	10% w/w	30min	RT
5	KCN	10% w/w	60min	RT
6	HNO_3	5% v/v	10min	RT
7	HNO_3	5% v/v	5min	RT
8	HNO_3	5% v/v	1.5min	RT

Table 3: KCN optimization

	Etchant	Time	Temperature
1	None (Reference)	-	-
2	10% w/w KCN	60min	RT
3	10% w/w KCN	90min	RT
4	20% w/w KCN	30min	RT
5	20% w/w KCN	60min	RT
6	30% w/w KCN	15min	RT
7	30% w/w KCN	30min	RT
8	30% w/w KCN	45min	RT

2.1.2 Chemical Bath Deposition of CdS

CdS thin films are a common component in various electronic and optoelectronic devices, especially as a promising heterojunction partner for polycrystalline chalcogenide photovoltaic materials such as CdTe and CIGS. In these photovoltaic devices, light should be able to penetrate the CdS layer and is absorbed in the p-type CZTSSe absorber layer to complete the pn-junction. Therefore, the CdS layer is kept as thin as possible, since light which is absorbed in the thick CdS layer decreases the overall photon absorption of a photovoltaic device. [19]
The most favored technique to synthesize polycrystalline films of CdS in photovoltaic thin film devices is chemical bath deposition, in which the CdS layer is deposited uniformly onto the CZTSSe surface. [20] The as-deposited CdS layer can be examined separately on a glass substrate to determine its film thickness, optical transmittance, or any other properties since it is relatively difficult to examine it on CZTSSe directly. The thickness of the CdS layer can be characterised using a profilometer on the CdS layer which was deposited on the glass substrate.

A small 50 ml beaker was placed in an oil bath which was heated up to 75 °C. 19.6 ml UPW were added to the beaker followed by 15 ml of 2 M NH_4OH. 1 ml of a 0.05 M $CdCl_2$ solution was added and the absorber samples

were placed in the beaker.
On the last stage, 4.4 ml of 1 M Thiourea were added to start the CdS reaction formation, which was indicated by the appearance of a yellow colour of the solution. The absorber layer and the glass were removed from the reaction solution after six minutes, rinsed with UPW and dried with N_2 gas.

2.1.3 Sputter Deposition

Direct Current (DC) sputtering is a physical vapor deposition method to fabricate thin film coatings of metals and metal oxides. A substrate which is to be coated is placed in a vacuum chamber, together with a target material which will act as the source of the coating material. In order to remove any residual water and air, the vacuum chamber will be first evacuated and then filled with high purity Argon. The DC, typically in the range of up to 5 keV, is applied to the target. The target will act upon the DC as the cathode point, which will eventually become the anode when a positive charge is applied to the to be coated substrate. Fast electrons are emitted as secondary electrons from the cathode. These secondary electrons are accelerated away from the cathode towards the anode. By collision of these electrons with the argon molecules a plasma is created which is the primary driving force to sputter the target material. Ionized argon molecules are accelerated onto the target material, causing the atoms to be "sputtered" off into a plasma. The vaporized atoms of the target material are then deposited when they condense as a thin film on the substrate. [21]

In this work, the ZnO, AZO and Ag layers were deposited with the Leybold UNIVEX450C Sputter System onto the sample consisted of stacked CZT(S,Se) and CdS on Molybdenum glass as the substrate. The parameters for the sputtering deposition are listed in Table 4.

Table 4: Materials and sputter parameter for the remaining components of the photovoltaic device.

Material	Thickness	Rate	Time
ZnO	50 nm	0.177 nm/s	282 s
AZO	40 nm	0.397 nm/s	101 s
Ag	7 nm	1.053 nm/s	7 s
AZO	50 nm	0.397 nm/s	126 s

2.2 Photovoltaic Device characterization

2.2.1 Solar Simulator

The primary characterization method to determine photovoltaic efficiency is by using a solar simulator.
A solar simulator produces illumination approximating natural sunlight in order to provide a controllable indoor test facility under laboratory conditions.
Standardized testing allows the comparison of devices manufactured at different companies and laboratories with different methods. The standards for cell testing are:

- Air mass 1.5 spectrum (AM 1.5) for terrestrial cells and Air Mass 0 (AM0) for cells, which are used outside the atmosphere, e.g. when used in space.
- Intensity of $1\,\mathrm{kW/m^2}$ or $1000\,\mathrm{mW/cm^2}$, also known as one-sun of illumination
- Cell Temperature of $25\,^{\circ}\mathrm{C}$ [22]

Current-Voltage measurements are a common method to examine electronic devices. As for the characterization of a PV device one can obtain five main electrical parameters from a light IV curve:

- $\mathrm{I_{SC}}$: The short circuit current ($\mathrm{J_{SC}}$, short circuit current density, when normalised to the cell area) is the current obtained from the solar cell when the voltage across the cell is 0 V. Therefore, the short-circuit current is the largest current which may be drawn from the solar cell. In Figure 11 it is the intercept of the y-axis.
- $\mathrm{V_{OC}}$: The open-circuit voltage is the maximum voltage attainable from a solar cell and occurs when the current through the device is 0. It is the intercept of the x-axis.
- $\mathrm{P_{max}}$: The maximum power point is the operating point of a solar cell at which the maximum power is provided. The power of a working point is equal to the surface $V*I$. This area must the be the maximum in case of $\mathrm{P_{max}}$. $\mathrm{I_{MPP}}$ and $\mathrm{V_{MPP}}$ are the current and voltage values which are associated with the maximum power point.
- FF: The fill factor describes the relationship of $\mathrm{P_{max}}$ to $\mathrm{P_T}$, which is the maximum power one can obtain from the PV device. $\mathrm{P_T}$ is the product of $\mathrm{V_{OC}}$ and $\mathrm{I_{SC}}$. In Figure 11 the fill factor is the ratio of the blue area to the yellow area.

$$FillFactor(FF) = \frac{V_{\mathrm{MPP}} * I_{\mathrm{MPP}}}{V_{\mathrm{OC}} * I_{\mathrm{SC}}} = \frac{P_{\mathrm{max}}}{P_{\mathrm{T}}} \tag{2}$$

- η: The efficiency is defined as the ratio of energy output from the solar cell to input energy from the sun. [5]

$$Efficiency(\eta) = \frac{P_{\mathrm{max}}}{P_{\mathrm{in}}} \tag{3}$$

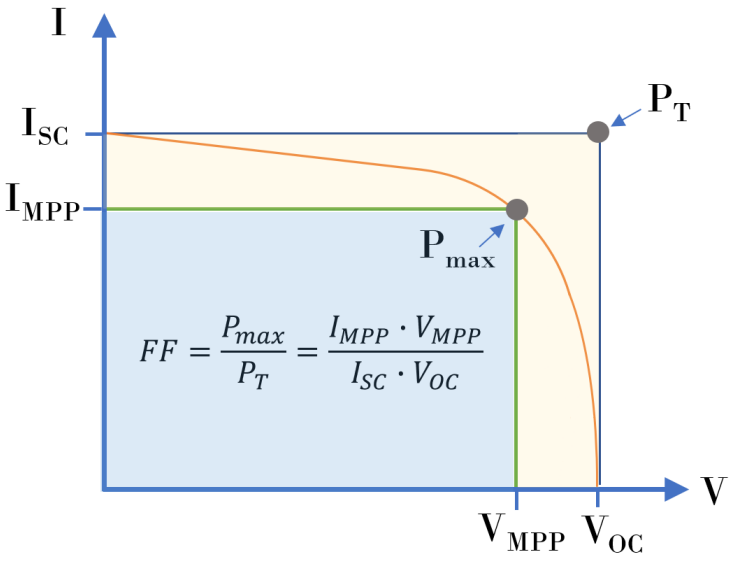

Figure 11: Typical I-V curve of a solar cell, shown as the orange curve.

2.2.2 External Quantum Efficiency

The measurement of the quantum efficiency (QE) is a common method to examine the PV efficiency of a solar cell. QE expresses the ratio of the number of photogenerated charge carriers (electrons) to the number of impinging photons. The QE is given as a function of wavelength or energy:

$$QE = \frac{electrons}{photons(\lambda)} \tag{4}$$

If all absorbed photons trigger the generation of a electron-hole pair, the value of QE is 1.
Two types of quantum efficiency are relevant for the characterization of solar cell performance: Whereas the External Quantum Efficiency (EQE) is defined as the ratio of generated electron-hole pairs to the overall incident photons, the Internal Quantum Efficiency (IQE) does not consider optical processes like transmission and reflection (R). [5] [23]

$$IQE = \frac{EQE}{1 - R} \tag{5}$$

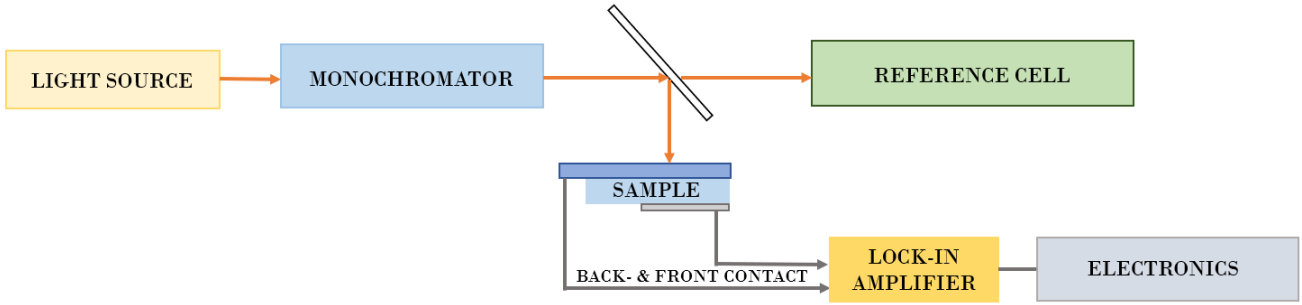

Figure 12: Components of a setup for quantum efficiency measurement.

Figure 12 shows the general setup of the quantum efficiency measurement. The system with which the EQE was measured in this thesis was the PVE300 setup by Bentham shown in Figure 13. The main setup components are listed:

- 1. Light Sources: Xenon and Quartz Tungsten Halogen. The light sources are positioned before the monochromator. Both light sources are being used to cover a wavelength range of 250-1800 nm.
- 2. Monochromator: the TMc300 monochromator provided by Bentham is a 300 mm focal length Czerny-Turner monochromator with a triple grating and a declared spectral range of 200 nm-50 μm. The monochromator is an optical device that transmits a selected narrow band of wavelengths of light chosen from a wider range of wavelengths available at the input.
- 3. A lock-in Signal Amplifier which amplifies the signal of the sample after illumination.
- 4. Dark Chamber: EQE measurements are performed in dark conditions since external light sources might influence the solar cell response.
- 5. Gold Test Plate: a gold chuck were the sample is positioned and contacted.
- 6. Probes to connect the sample.

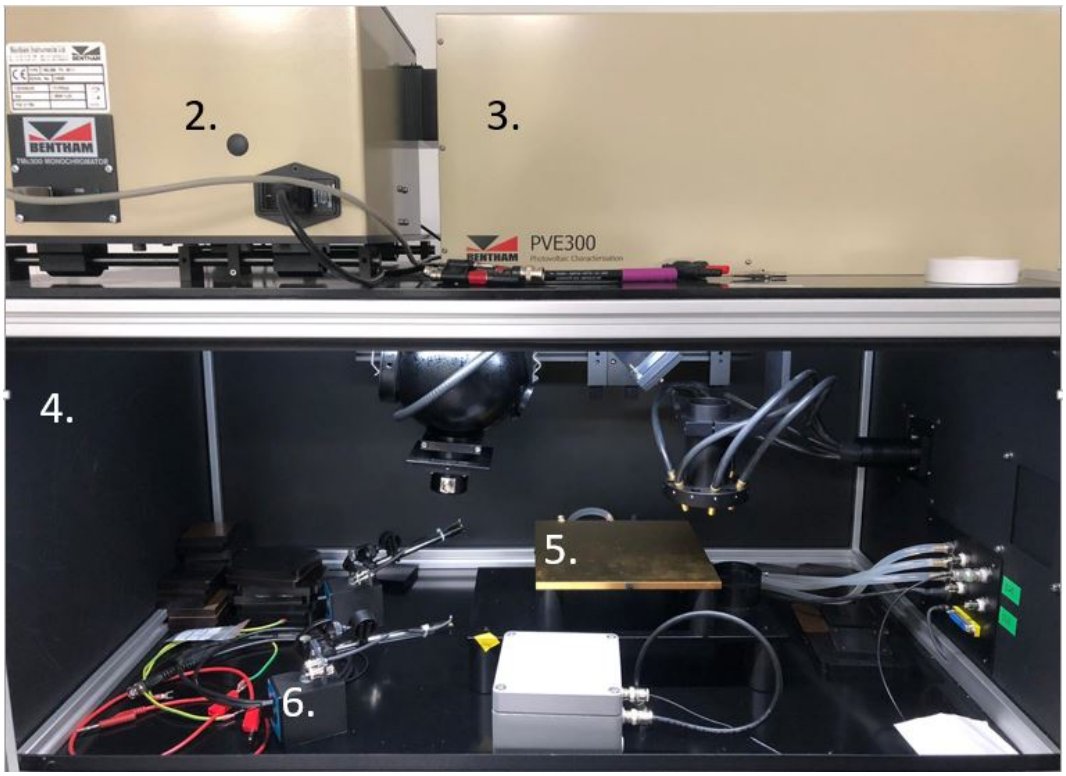

Figure 13: Measurement setup of the EQE Measurement.

The sample was placed onto the cooled chuck and contacted with the pins of the end of the probes, performing a 2-point measurement. The temperature of the test plate is controlled by a water circuit. The cell is positioned under the vertical light beam and connected to the amplifier. The nominal dimension of the light beam used for the measurements is 0.74x0.74 mm^2.

The data are automatically acquired by Benwin+ software provided by Bentham. The solar cells spectral responsivity (SP) spectrum was measured between 300 nm and 1800 nm, using a wavelength step of 5 nm. Benwin+ software automatically converts the SR spectrum into EQE spectrum.

2.2.3 Scanning Electron Microscopy

Scannning Electron Microscopy (SEM) is one the most widely used high resolution imaging instruments which finds its application in various fields such as imaging and chemical analysis for materials of all types.
To create an image, electrons are extracted from an electron source which are then accelerated to form an electron beam with an energy varying from 100 eV up to 30 keV, also known as the primary electron beam. The trajectory of accelerate electrons is controlled by an anode which attracts the electrons. When primary electrons are focused using a condenser and an objective lens, the imaged area is irradiated by the electron beam. By using scanning coils, one can control a sequential scanning pattern in a linear raster pattern across the region of interest. The image is generated by the interaction of the incident beam electrons with the sample atoms which can result in either elastic or inelastic scattering: in inelastic scattering, the incident electrons are deflected without any loss of energy whereas inelastic scattering involves a loss of energy resulting in the ionization of the sample atoms. The region in which one can find the scattered electrons (both elastic and inelastic) is the interaction volume. Two important signals which are to be detected in SEM are secondary electrons (SE) and back-scattered electrons (BSE). When the incident beam causes electrons to be ejected from the sample, these electrons are called SE and are relatively low in energy with less than 25 eV. Contrarily, BSE are incident electrons from the primary electron beam that have been scattered multiple times and emerge again from the sample surface. Therefore, SE allow a strong topographical imaging of the sample surface and BSE provide a compositional contrast as the strength of the BSE depends strongly on the atomic number of the sample atoms. Most SEM instruments utilize different kinds of detectors in order to detect SE and BSE separately. [24]

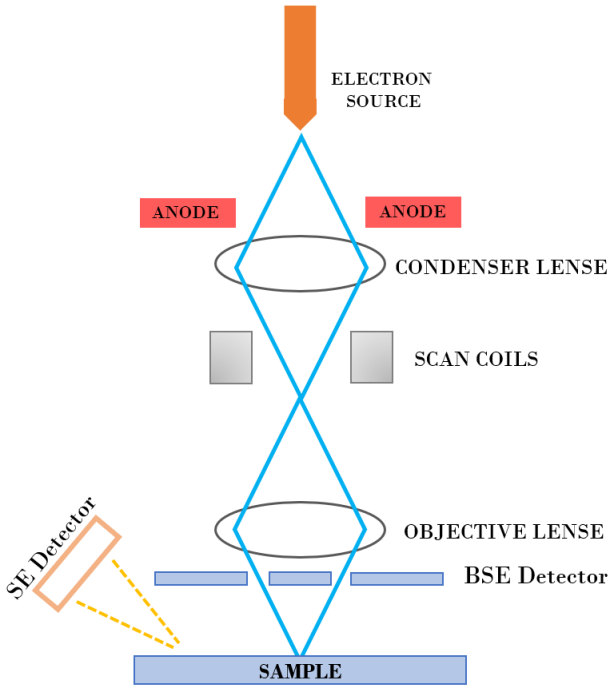

Figure 14: Basic components of a scanning electron microscope.

2.2.4 Raman Spectroscopy

Raman spectroscopy is a type of vibrational spectroscopy used for the analysis of various sample types (e.g. gases, liquids, powders and films). It can be performed for a identification of a sample specimen, by examining the vibrational modes of a molecule. In general, Raman spectroscopy utilizes light scattering induced by symmetric or in-phase vibrations of non-polar groups. Scattered light photons usually consist mostly of Rayleigh scattered light and only a small amount of Raman scattered light. While elastically scattered Rayleigh light loses no energy in the process, Raman scattered light loses energy relative to the exciting energy. Both processes, Rayleigh and Raman, are two photon processes which involve scattering of the incident light from a virtual state. A new photon is created and scattered from this virtual state when the incident photon is momentarily absorbed by a the transition from ground onto virtual state.

Raman scattering, with an observed intensity of 10^{-6} of the incident light is relatively less probable than Rayleigh scattering, which has a more dominant intensity with 10^{-3} of the incident light. In case of Rayleigh, the scattered photon is generated by the transition from the virtual state back to the ground state without any loss of energy. In contrary to that, a Raman scattered photon will have a different energy and frequency when transitioned back from virtual state into ground state due to an inelastic collision between photon and molecule. Raman vibrational bands are mainly identified by their frequency and the intensity which depends on the polar character of the molecule. The vibrational energy levels are unique to each molecule, therefore Raman spectroscopy can provide a "fingerprint" identification of a particular molecule. Since the frequencies of molecular vibrations depend on the masses of the atoms, their bonds and geometric alignment, Raman spectra can provide useful information on the molecular structure and environment of a molecule. [25].

Most Raman instruments use light from a high intensity laser. In order to distinguish Raman scattering from Rayleigh scattering, a Rayleigh filter is used. Raman scatter is obtained perpendicular to the laser source and detected with an array detector or a charged-couple-device.

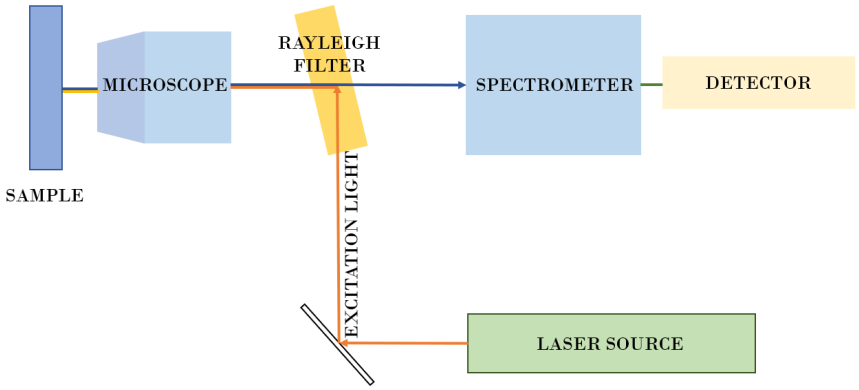

Figure 15: Components of a Raman Spectrometer.

The CZT(S,Se) absorbers in this work were examined using Raman spectrometer WITec alpha 300A at the Nanocentre of the University of Vienna. All samples were examined using a laser excitation wavelength of 532 nm and a laser power of 3.813 mW.

2.2.5 X-Ray Diffraction Analysis

X-ray diffraction analysis (XRD) is a non-destructive and widely used technique to determine characteristic parameters of a crystal such as phase identification, lattice orientation and overall crystallographic structure of a solid material. X-rays are electromagnetic radiations within the range of 10^{-3} nm to 10 nm, making them much shorter than the wavelength of visible light (380-700 nm). This allows X-rays to penetrate through materials that are optically opaque, e.g. metals.
Within a crystal, atoms are arranged periodically. Since X-rays have wavelengths which are similar to the size of atoms, one can observe an interaction in a form of diffraction of the X-rays. Thus, X-ray diffraction can be considered a scattering phenomenon involving a larger number of atoms which are periodically arranged. The scattered X-rays can be in-phase resulting in either destructive or constructive interference. In case of constructive interference, the waves add in specific directions, given by Bragg's law:

$$2dsin\theta = n\lambda \tag{6}$$

d... spacing between diffracting planes
θ...incident angle
n... positive integer
λ... beam wavelength

The peak intensities are determined by the periodic arrangement of the atoms within a unit cell. The X-ray diffraction can be considered as characteristic and provide a "fingerprint" identification using a standard database of X-Ray diffraction pattern, also known as Crystallography Open Database (COD). [26]

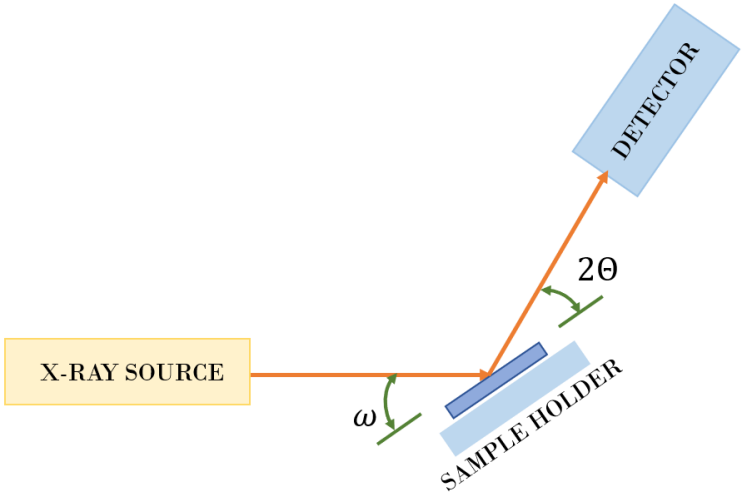

Figure 16: Schematic overview of an X-ray diffraction analysis instrument. 2θ refers to the angle between the incident and the then diffracted X-Ray beam and ω is defined as the angle between the incident X-Ray beam and the sample holder.

3 Results and Discussion

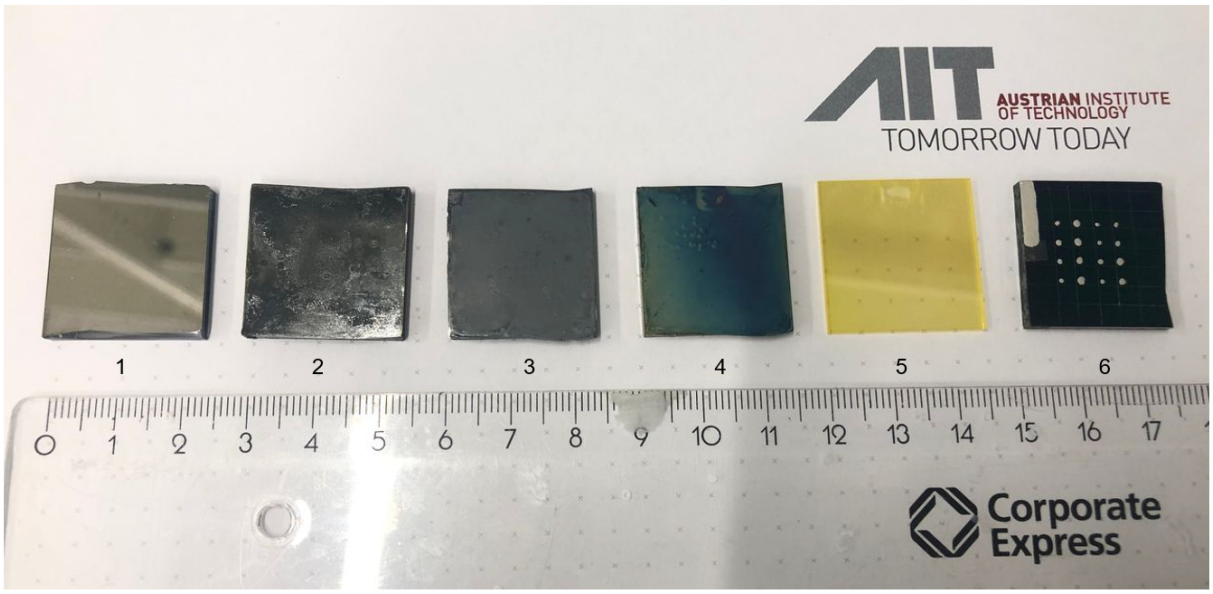

Figure 17: A representative of processing stages of kesterite CZTSSe photovoltaic device fabrication. (Left to right) 1: Mo-coated soda lime glass, 2: as-deposited spin coated CZTS-precursor solution, 3: as-annealed CZT(S,Se), 4: as-deposited CdS using chemical bath deposition, 5: as-deposited CdS using chemical bath deposition on glass substrate for separate investigations, 6: full functioning kesterite CZT(S,Se) photovoltaic device with i-ZnO window layer and AZO-Ag-AZO front electrode, mechanically scribed into 3 x 3 mm cells and contacted with conductive Ag-paste.

All processing stages of the kesterite CZT(S,Se) photovoltaic device fabrication are shown in Figure 17: the first sample (1) shows a cleaned Mo-coated soda lime glass substrate. In the next step (2), the precursor solution was deposited via spin-coating and subsequently annealed at 620 °C (3). A thin film of CdS as a buffer layer was deposited onto the kesterite CZT(S,Se) absorber in a process of chemical bath deposition (4), in which a glass substrate was placed simultaneously (5) for additional analysis of the CdS layer. The thickness of the CdS layer was determined using a profilometer and turned out to be 51.44±5.71 nm. After the sputter deposition of the window layer of i-ZnO/AZO/Ag/AZO the photovoltaic device was mechanically scribed into 3x3 mm cells and connected using a Ag-paste for photovoltaic characterization methods (6).

3.1 Absorber Layer Preparation and characterization

3.1.1 Secondary Phase Analysis

The kesterite CZT(S,Se) absorber was successfully fabricated using the spin coated precursor ink and subsequent annealing under sulfur vapor at 620 °C.
Figure 18 shows the cross-section as well as the surface of kesterite CZTS. The secondary phase can be noticed as bright spots which are mainly located on the CZTS surface at the grain boundaries, encircled in a) and b). These bright spots are later in this thesis identified as Cu_2S and/or ZnS using XRD and Raman spectroscopy.

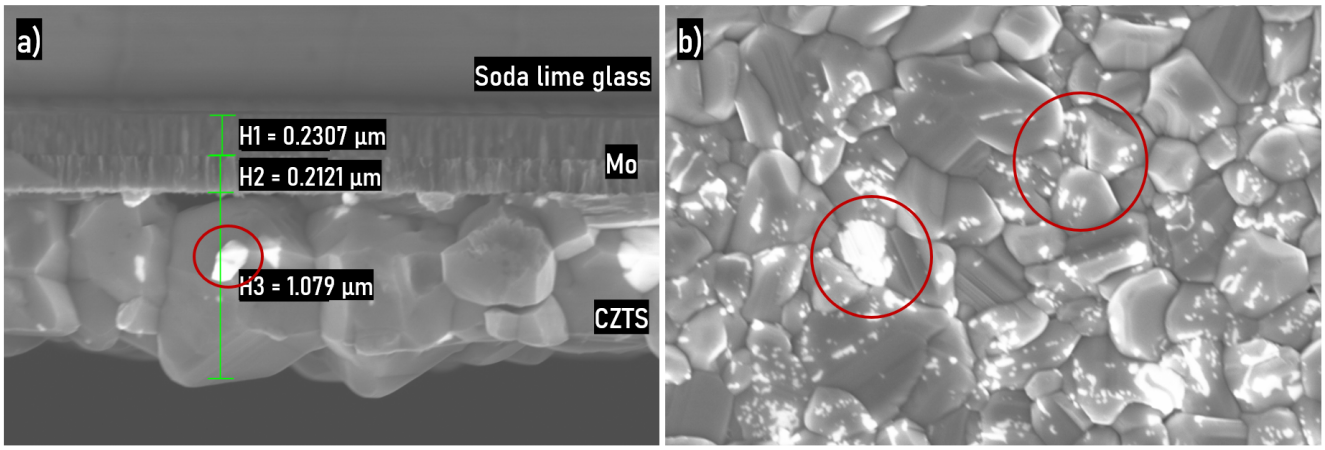

Figure 18: a) SEM image of the cross-section of an as-annealed kesterite CZTS absorber layer. The thickness can be determined using SEM. b) SEM image of the as-annealed kesterite CZTS surface. The bright spots are considered as a secondary phase which is likely to be Cu_2S or ZnS.

3.1.2 Effect of Selenium to Sulphur Ratio

Figure 19 shows the visual effects on the kesterite absorber layer when the Se content was increased in the annealing process. It is worth mentioning that the kesterite grains increase in size with increasing amount of Se. Additionally, all samples have visible superficial secondary phases which again appear as white brights spots on the SEM images.

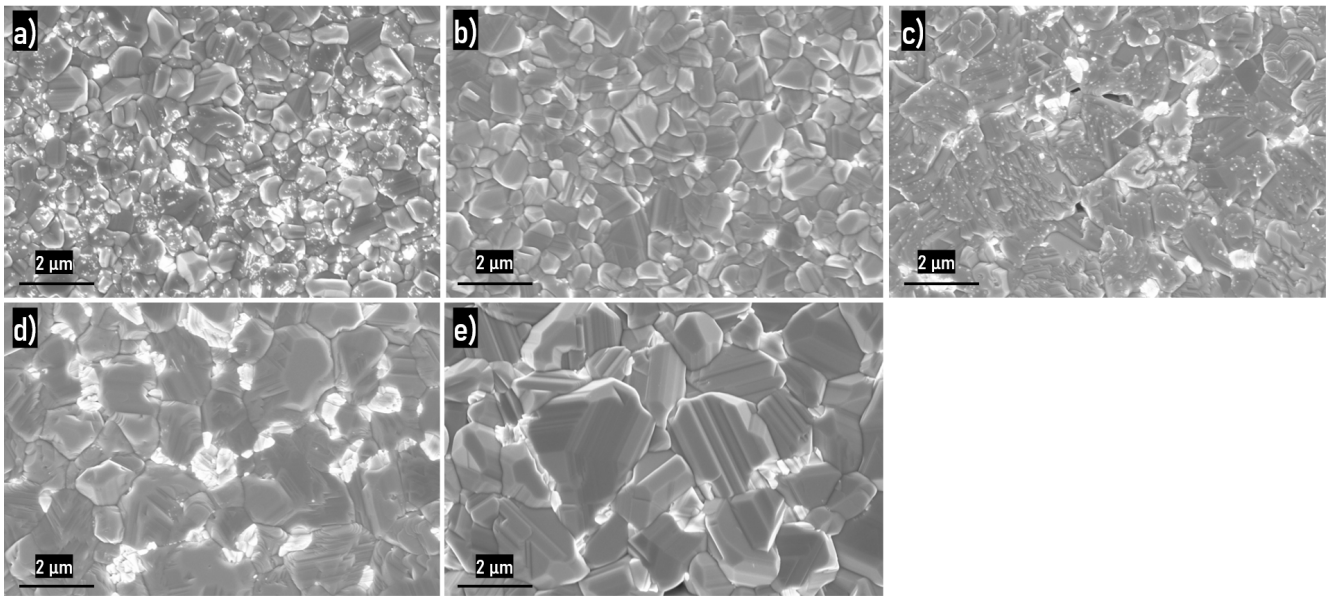

Figure 19: a) SEM image of CZTS (x=0) surface. b) SEM image of CZTSSe (x=0.25) surface. c) SEM image of CZTSSe (x=0.5) surface d) SEM image of CZTSSe (x=0.75) surface. e) SEM image of CZTSe (x=1) surface.

The X-Ray diffractogram of a kesterite CZTS (x=0) on Mo-coated soda lime glass in Figure 20 shows the presence of Cu_2S secondary phase. One can notice signals at $2\theta = 32$ and $2\theta = 54$ which can not be associated with the CZT(S,Se) characteristic XRD signals which are shown in the upper right corner. According to the crystallographic open database (COD) 96-153-0509 one can find that the signals found at $2\theta = 32$ and $2\theta = 54$ can be classified with Cu_2S, which appears as a secondary phase on the kesterite CZTS surface.
In regards of further investigations on secondary phases, the characteristic signals of ZnS secondary phases overlap with the characteristic signals of CZTS and can therefore not be detected using XRD on a CZTS surface. This is due the identical crystal structure between tetragonal kesterite and cubic sphalerite/zincblende ZnS. The tetragonal kesterite CZTS consists of a stack of two cubic sphalerite in z (vertical) direction.

In order to distinguish ZnS phase from CZTS one, Raman spectroscopy was incorporated. It is also useful to confirm the XRD results on particular secondary phases such as Cu_2S and SnS.

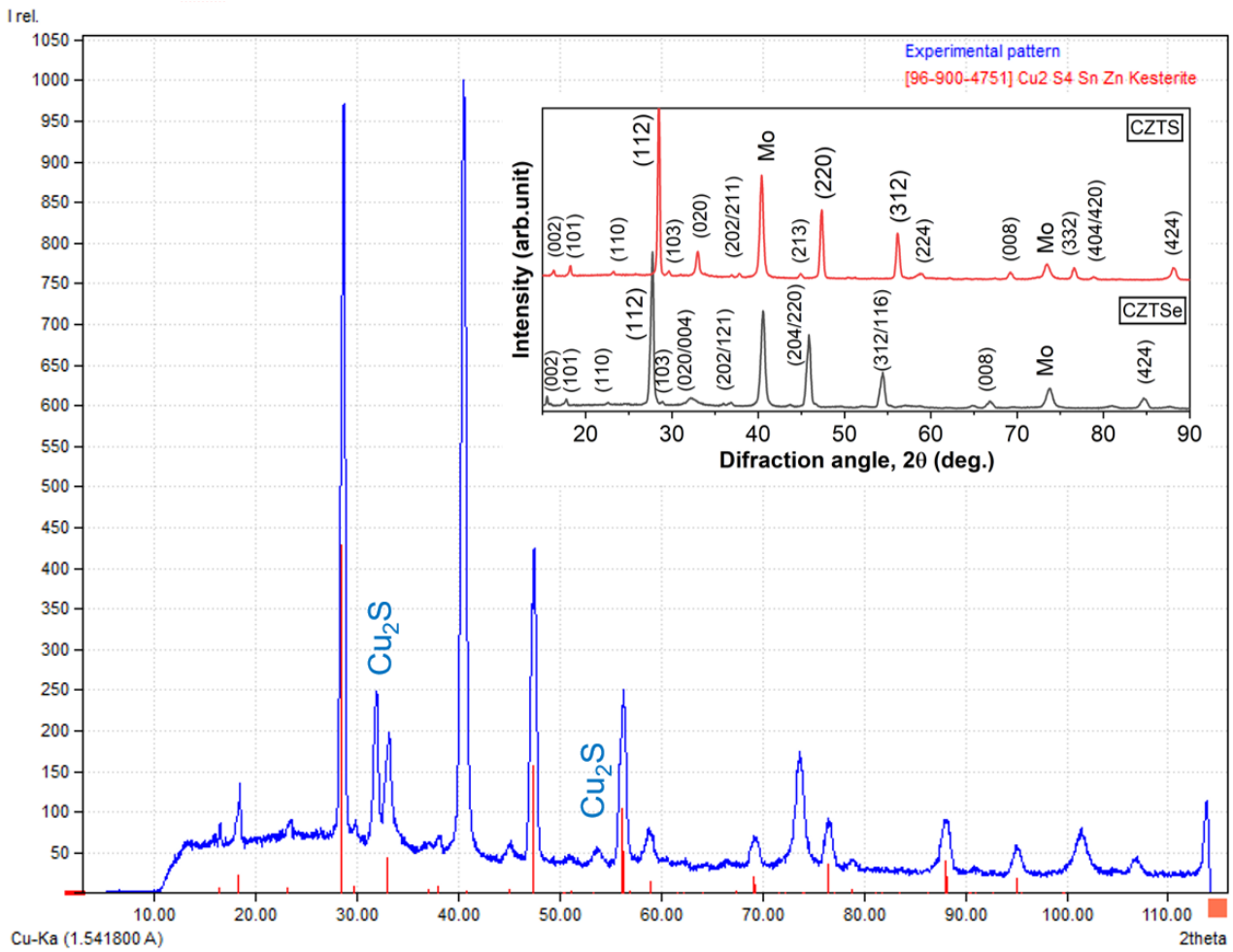

Figure 20: X-Ray Diffractogram of kesterite CZTS (x=0) on Mo-coated soda lime glass. The characteristic signals of Cu_2S are marked at $2\theta = 32$ and $2\theta = 54$. In the upper right corner one can see a XRD diffractogram of pure CZTS and CZTSe on Molybdenum as a reference.

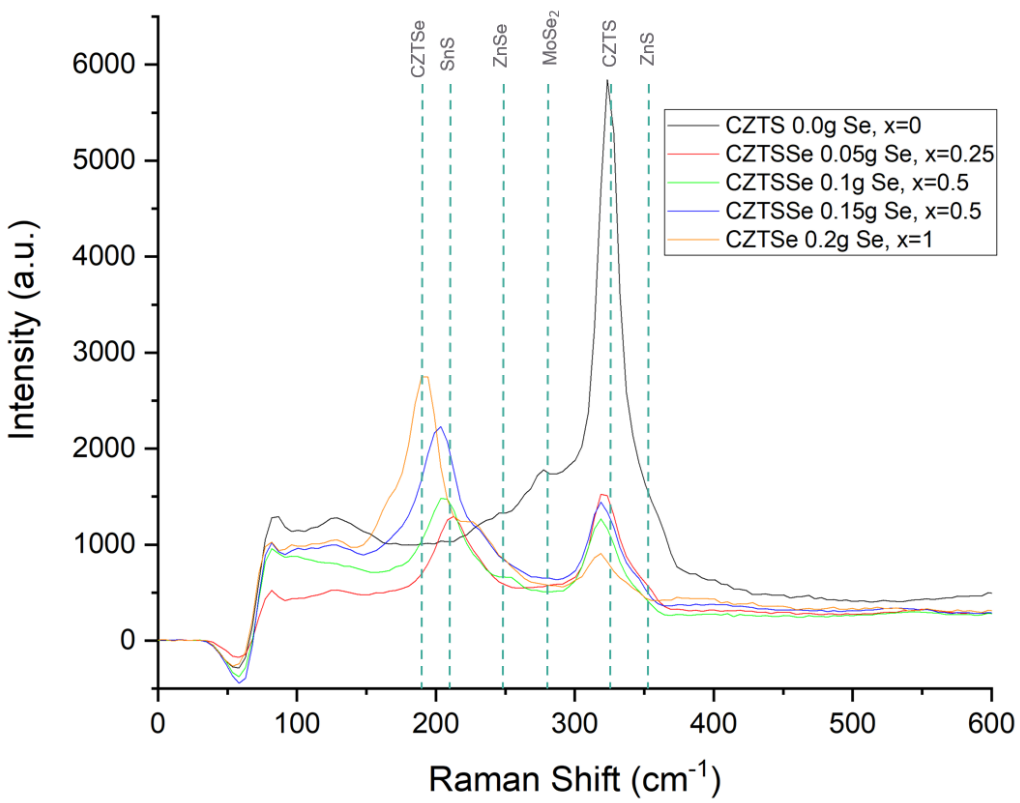

Figure 21: Raman spectra of kesterite CZTSSe x=0-1.0. The vertical dashed lines illustrate the Raman signals of the phases that are expected at a certain Raman Shift.

The Raman spetra of the CZT(S,Se) samples are shown in Figure 21. To easily identify the different bands, the position of the signals of CZTS, CZTSe, as well as potential secondary phases are illustrated using a dashed green line: The signals of CZTS can be found at 338 cm^{-1}. As the amount of Se in the CZTSSe absorbers increase, one can see that the signals shifts from 338 cm^{-1} towards 196 cm^{-1}, where the characteristic signal of CZTSe can be found. Raman signals of secondary phases such as SnS (217 cm^{-1}), ZnS (353 cm^{-1}), ZnSe (253 cm^{-1}) are also marked. [27] [28] [29]

It is clear that none of the samples consist solely of CZTSe as even the CZTSe (x=1) absorber shows a small signal of CZTS due to the Thiourea in the precursor solution. A small shoulder at 352 cm^{-1} suggests the possible existence of ZnS at the kesterite surface on all samples.

3.2 Chemical Etching of Absorber

3.2.1 Effects of Etching on CZTS with KCN and HCl

In the following experiments CZTS (x=0) absorber samples with 9 cycles of spin coating prior to the annealing process were chemically treated with etchants to remove unwanted secondary phases. The CZTS samples were etched with either 10 % w/w KCN for 60 min at room temperature or with 10 % v/v HCl for 10 min at 75 °C. The effects of etching were examined using SEM and XRD. Additionally, CZTSSe x=0.25-1 samples were etched with 10 % HCl and examined before and after etching using Raman spectroscopy.

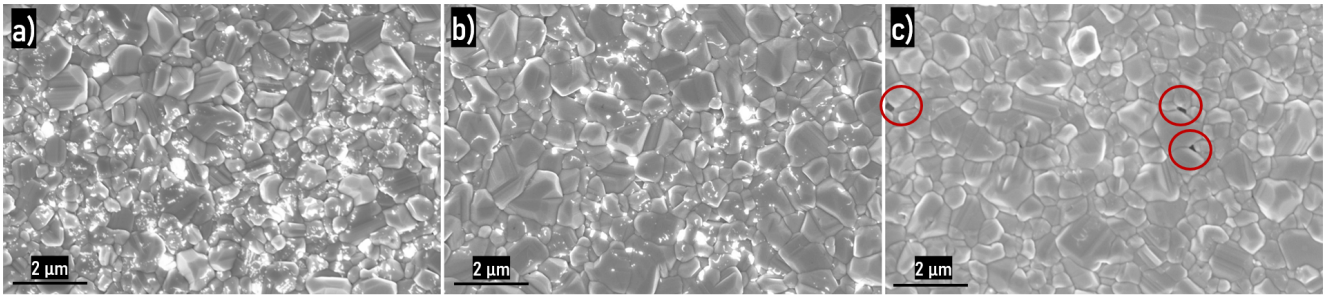

Figure 22: a) SEM image of kesterite CZTS surface as a reference. b) SEM image of kesterite CZTS surface after etching with 10 % w/w KCN for 60min at RT. c) SEM image of kesterite CZTS surface after etching with 10 % v/v HCl for 10 min at 75 °C.

As seen in Figure 22 the number of secondary phases, shown as bright superficial spots on CZTS grains, are notably reduced with the KCN as with the HCl. The bright spots of secondary phases seem to be located on the grain boundaries of CZTS. This suggests that the secondary phases form from a segregation mechanism that occurs on the CZTS grain boundaries. The surface of image c) in Figue 22 shows no secondary phase at all, but one can notice some pores (encircled in red in c)) where the secondary phases were supposedly located prior to etching. These pores appear as a result from the removal of secondary phases by the etching process from the CZTS grain boundaries.

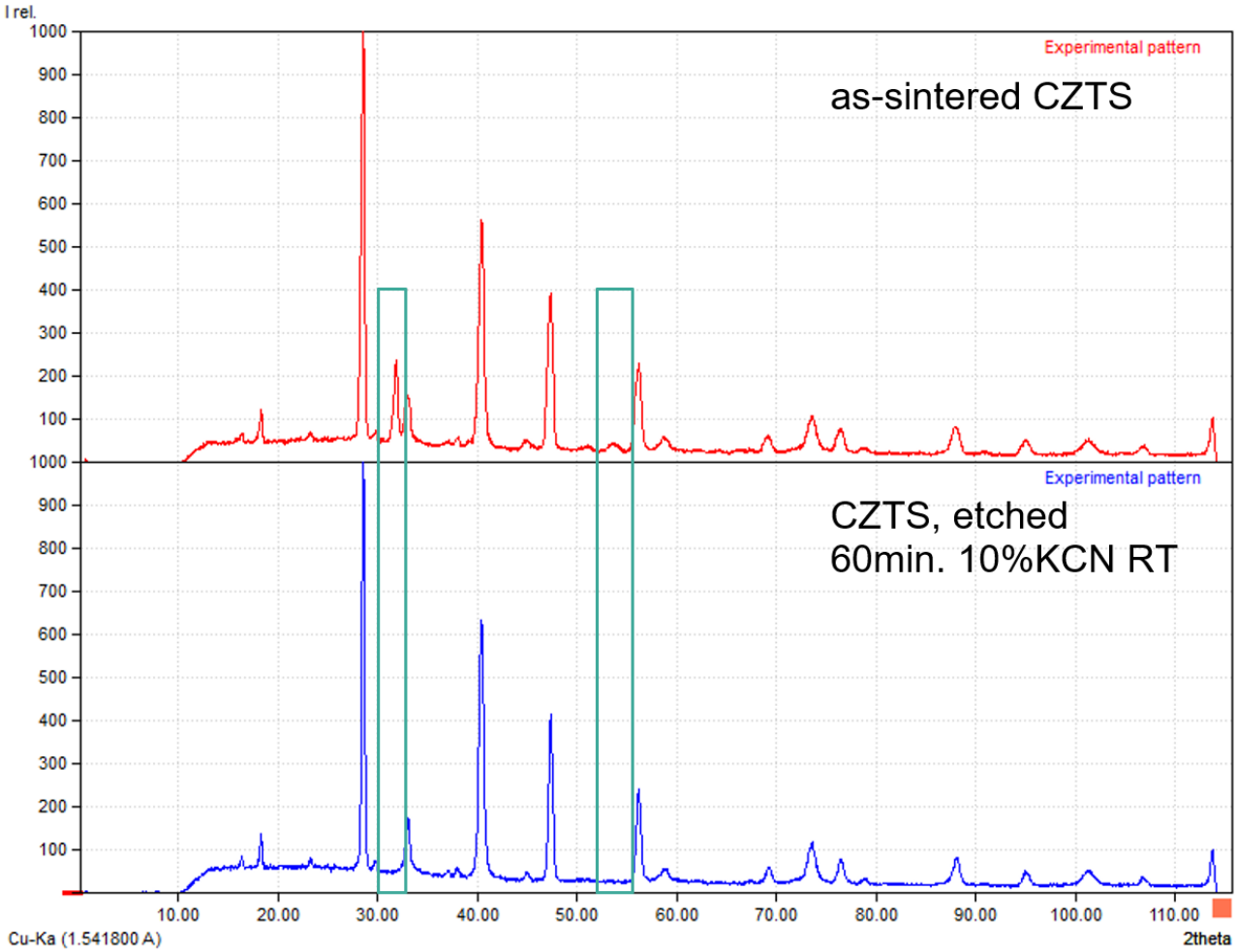

Figure 23: X-Ray Diffractogram of kesterite CZTS on Mo-coated soda lime glass before and after etching with 10 % w/w KCN for 60 min at RT. The green bars at $\theta = 32$ and $\theta = 54$ mark the characteristic signals of Cu_2S secondary phase.

Both chemical etching treatments, the KCN as well as the HCl, successfully removed Cu_2S on the kesterite CZTS absorber layer as seen in Figure 23 and in Figure 24. In both diffractograms, the characteristic signals for Cu_2S disappear after an etching treatment. The difference caused by the etching treatments are emphasised using a green bar to show the characteristic signals of Cu_2S secondary phases before and after etching.

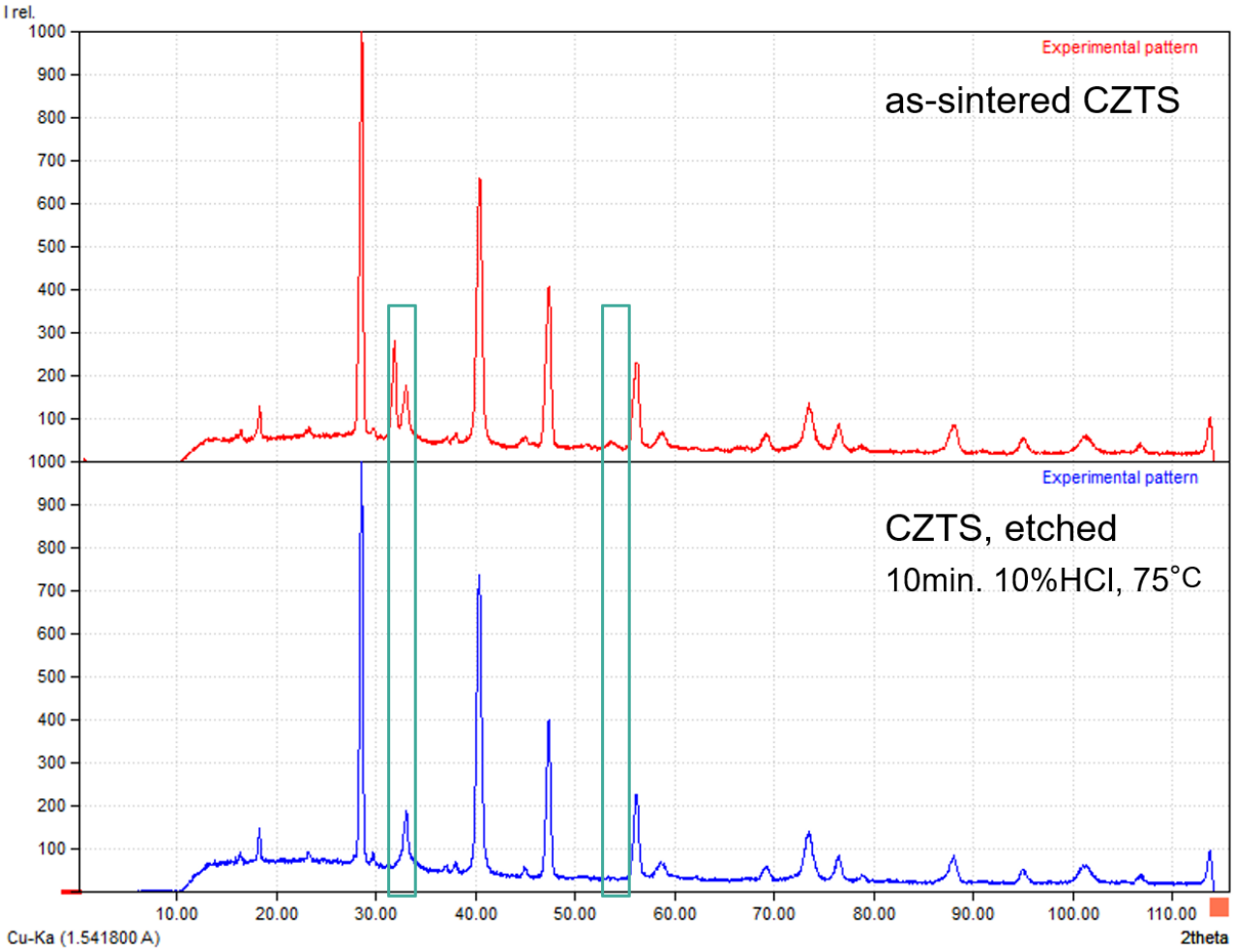

Figure 24: X-Ray Diffractogram of kesterite CZTS on Mo-coated soda lime glass before and after etching with 10 % v/v HCl for 10 min at 75 °C. The green bars at $\theta = 32$ and $\theta = 54$ mark the characteristic signals of Cu_2S secondary phase.

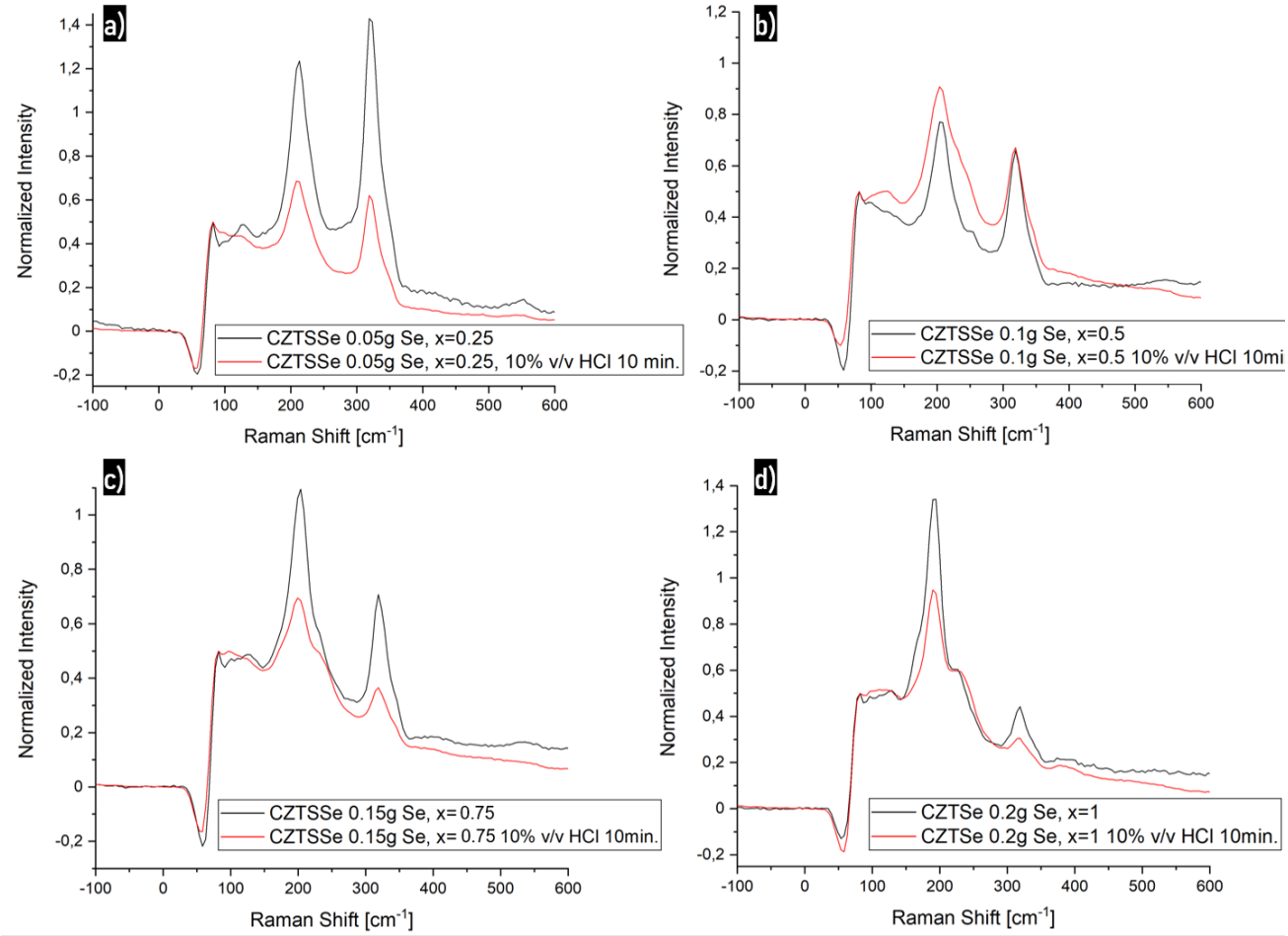

Figure 25: a) Raman spectrum of kesterite CZTSSe x=0.25 absorber layer before etching, illustrated in black, and after etching with 10 % v/v HCl for 10 min at 75 °C, illustrated in red. b) Raman spectrum of kesterite CZTSSe x=0.5 absorber layer before etching, illustrated in black, and after etching with 10 % v/v HCl for 10min at 75 °C, illustrated in red.c) Raman spectrum of kesterite CZTSSe x=0.75 absorber layer before etching, illustrated in black, and after etching with 10 % v/v HCl for 10 min at 75 °C, illustrated in red. d) Raman spectrum of kesterite CZTSSe x=1 absorber layer before etching, illustrated in black, and after etching with 10 % v/v HCl for 10 min at 75 °C, illustrated in red.

The CZTSSe samples were examined with Raman spectroscopy at the University of Vienna prior to the etching, brought back to the AIT for etching and once again after etching to ensure the examination of the etching effects on the same sample. The spectra were normalized by setting the first detectable signal at 89 cm^{-1} equal to 0.5 . The effects of the 10 min 10 % v/v HCl etching treatment are exhibited visibly in the Raman spectra in Figure 25: The characteristic signals for CZTS and CZTSe, which are located at 196 cm^{-1} and 338 cm^{-1}, and the signal for CZTSSe (x=0.25 therefore at 205 cm^{-1}) both decreased significantly after etching treatment, leading to the assumption that the etching process with 10 % v/v HCl also damages the kesterite surface structure. One exception can be taken from Figure 25 b) as the signal for the CZTSSe absorber sample has not been as dominant

as the other samples since the peaks, even though normalized, are not as high compared to the samples in a), c) and d). Furthermore, the etching does not lead to any other effects, other than decreasing the charasteristic signals of the CZTSSe absorbers. It can therefore be assumed, that the HCl in general is not a suitable etchants for a selective removal of any detectable secondary phase on CZTSSe.

3.3 PV Device characterization

3.3.1 Different Selenium to Sulphur Ratio

I-V and EQE Measurement

PV devices with different ratios of Se/S were examined using state-of-the-art tools for PV characterization. By the practice of Current-Voltage measurements of the PV device it was managed to determine the best working cell of each PV device according to their PV efficiency. This cell was then preferably selected for the measurement of the external quantum efficiency.

All samples with only Sulphur content (x=0) to mostly Selenium content (x=1) were fully functioning as absorber components in photovoltaic devices: The I-V curves are shown in the Figure 26, whereas the left hand side shows the I-V curves of unetched PV devices and the right hand side shows the I-V curves of PV devides which have been etched with 10 % v/v HCl for 10 min. The different ratios of Sulphur to Selenium effect the short-circuit-current density represented as the intercept of the y-axis as the short-circuit density increases with Se content. However, the performance of all PV devices dropped when the absorber layer was chemically etched with 10 % v/v HCl for 10 min at 75 °C, which was intended to remove secondary phases selectively. It can even be assumed when comparing the curves in Figure 26, that the chemical etching destroyed the PV devices as no measurements could have been performed on the PV devices with CZTS (x=0) and CZTSe (x=1) absorber. Furthermore, if the PV efficiency in Table 5 is compared to the PV efficiency in Table 6, the HCl etchant seems to reduce the performance of the CZT(S,Se) cells. The assumption that the HCl etchant destroys the CZT(S,Se) surface is supported by the data obtained by the surface-sensitive Raman spectroscopy performed previously in Figure 25. The surface damage due to HCl etching could form the non-ideal interface between CZT(S,Se) and CdS that leads to a higher series resistance and low shunt resistance of the cells, as presented in the Table 5 and Table 6 as well, yielding cells efficiency reduction.

In addition, increasing the Selenium content in the preparation of the kesterite CZT(S,Se) absorber layer affects the overall performance due to the variation of the band gap leading to different photon absorption, which can be clearly seen in Figure 27 as the band gap decreased with increasing Se content, the absorption range becomes broader.

Nevertheless, from the I-V curves in Figure 26 and from the Table 5 it can be obtained that in both cases, etched and unetched absorber component, a Se/S ratio of x=0.25 performed best with a PV efficiency of 4.8 %, which dropped to 2.4 % when the absorber is etched. Therefore, in the following experiments, only PV devices with CZTSSe x=0.25 kesterite absorber were examined for further investigations and examinations.

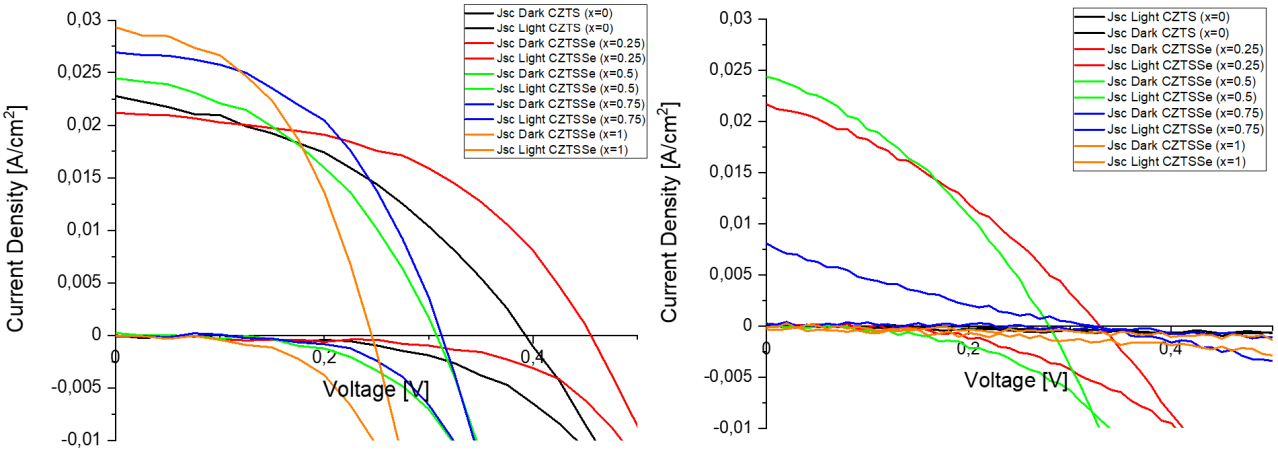

Figure 26: Current-Voltage (I-V) measurement of photovoltaic devices with different Se/S ratios in kesterite absorber before and after the kesterite absorber layer was chemically treated with with 10 % v/v HCl for 10 min at 75 °C.

Table 5: Resulting data from I-V measurement of different CZTSSe compositions as absorber layers in PV device.

Cell Name	Se/S ratio	Efficiency, %	V_{OC}, V	J_{SC}, mA/cm^2	FF, %	P_{max}, W	R_{shunt}, Ω	R_{series}, Ω
D4	CZTS (x=0)	3.4	0.39	21.06	41.08	0.000253	326.330	8.097
C5	CZTSSe (x=0.25)	4.8	0.45	21.11	49.98	0.000356	248.820	6.027
C4	CZTSSe (x=0.5)	3.2	0.30	24.50	43.62	0.000242	301.920	4.680
E3	CZTSSe (x=0.75)	4.0	0.31	27.01	48.39	0.000301	207.615	3.871
C5	CZTSe (x=1)	3.3	0.24	28.99	47.85	0.000248	191.594	2.603

Table 6: Resulting data from I-V measurement of different CZTSSe compositions as absorber layers in PV device after etching with 10 % v/v HCl for 10 min at 75 °C.

Cell Name	Se/S ratio	Efficiency, %	V_{OC}, V	J_{SC}, mA/cm^2	FF, %	P_{max}, W	R_{shunt}, Ω	R_{series}, Ω
D2	CZTS (x=0)	-	-	-	-	-	-	-
C3	CZTSSe (x=0.25)	2.4	0.33	21.48	34.35	0.000170	142.480	9.269
B2	CZTSSe (x=0.5)	2.4	0.28	24.38	35.37	0.000168	116.410	5.930
C4	CZTSSe (x=0.75)	0.5	0.32	8.03	19.68	0.000036	290.008	9.265
C2	CZTSSe (x=1)	-	-	-	-	-	-	-

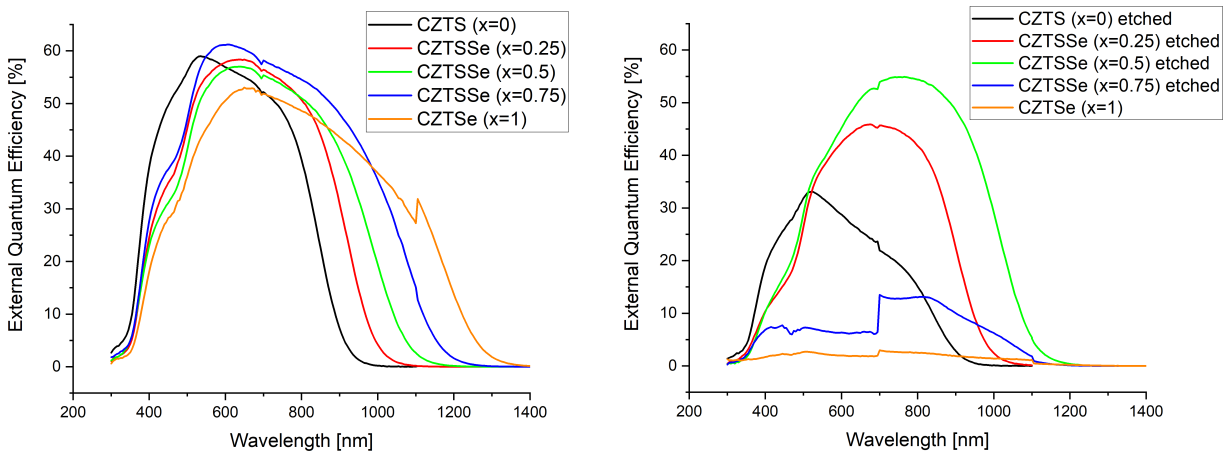

Figure 27: (Left) Measurement of External Quantum Efficiency of different CZTSSe compositions as absorber layers in PV device before and (Right) after etching with 10 % v/v HCl for 10 min at 75 °C.

The EQE measurements in Figure 27 reveal the damage of the CZTSSe absorber layers with increasing amount of Se content. In addition, by the increase of the Se content in the absorber, one can observe a noticeable shift in the upper absorption range of the EQE measurements: as the Se content increases, the band gap decreases and as a result, the absorption range becomes broader. An additional effect of the increasing Se content in the absorber is the decrease of the open-circuit voltage V_{OC} in Table 5. One can also notice the photon absorption of ZnO and CdS which is to be expected at 350 nm and 450 nm. [30]

3.4 Optimization Process

3.4.1 Thickness

At first the absorber was examined on its thickness. A thickness of at approximately 1.3 µm was striven for which delivers the best solar cell efficiency due to the prevention of recombination of the photo-generated carriers which recombines before reaching the buffer layer/CZTS layer interface. [31]
The first samples were CZTS absorber layers with 9 cycles of spin coating. The thickness was determined by examining the film cross section of the sample under the SEM and measuring the thickness.

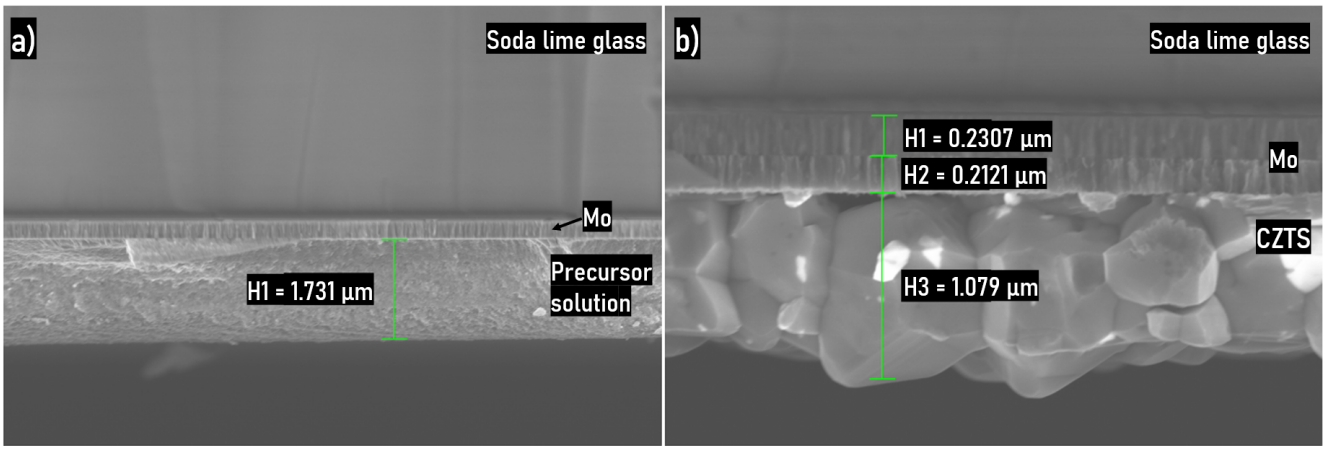

Figure 28: a) 9 spin-coated layers of the as-deposited CZTS-precursor solution on Mo-coated soda lime glass. b) as-annealed CZTS kesterite absorber layer on Mo-coated soda lime glass.

As seen in Figure 28 the thickness of the kesterite CZTS absorber decreased after sintering from a thickness of 1.731 μm to 1.079 μm.
In the following experiments 6 CZTSSe (x=0.25) absorber layer samples were prepared with 9-14 cycles of spin coating and subsequent annealing. The absorbers were cut in half to obtain a cross-section which was then examined using SEM to measure the kesterite thickness.

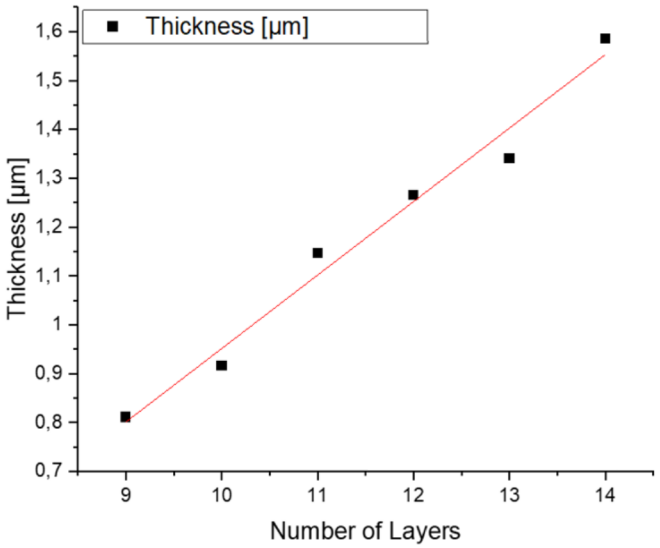

Figure 29: Thickness of the as-annealed kesterite CZTSSe absorber layer with 9-14 cycles of spincoating.

As it can be taken from Figure 29 the as-annealed kesterite CZTSSe absorber increased in thickness with increasing number of spin coating cycles. In further experiments, the PV device characterization was continued with exclusively CZTSSe x=0.25 with 12 cycles of spin coating.

3.4.2 Effects of Different Etchants on Absorber Layer and PV Device Performance

The experiments in which the kesterite absorber layers were chemically etched with 10 % v/v HCl for 10 min at 75 °C was only effective according to the SEM images of the kesterite surface in Figure 22 since no secondary phases could have been detected on the surface. Nevertheless, the use of 10 % v/v HCl for 10 min at 75 °C as an etchant decreased the performance of the PV device significantly which is clearly described in Figure 26 and Table 6.

As HCl was still sufficient in removing the secondary phase a lower concentration such as 5 % v/v HCl and shorter amounts of etching time were investigated as well as the effects of 10 % w/w KCN and 5 % v/v HNO_3.

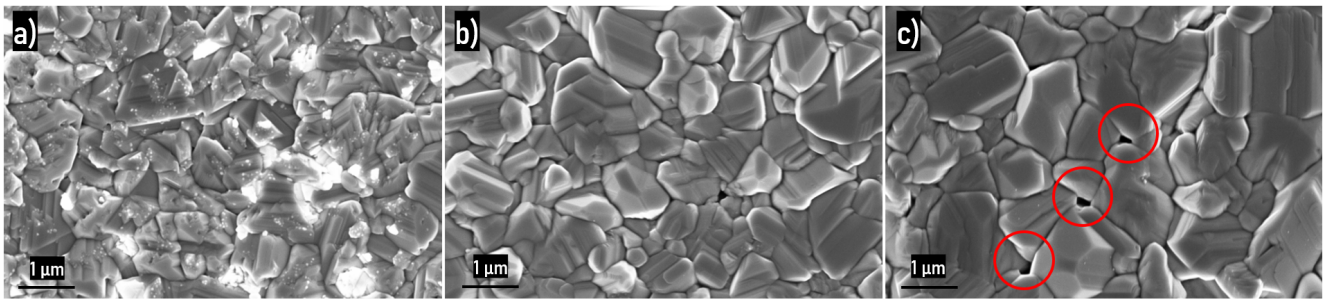

Figure 30: a) SEM image of kesterite CZTSSe surface as a reference. b) SEM image of kesterite CZTSSe surface after etching with 5 % v/v HCl for 30 s at 75 °C. c) SEM image of kesterite CZTSSe surface after etching with 5 % v/v HCl for 60 s at 75 °C

As expected due to previous experiments, as seen in Figure 30 the HCl successfully removes any superficial secondary phases but leaving behind pores, which are encircled in red in c), on spots on which a secondary phase was supposedly located before any etching treatments. HCl removes the secondary phase even with a low concentration of 5 % v/v and a shorter amount of etching time such as 30 s and 60 s.

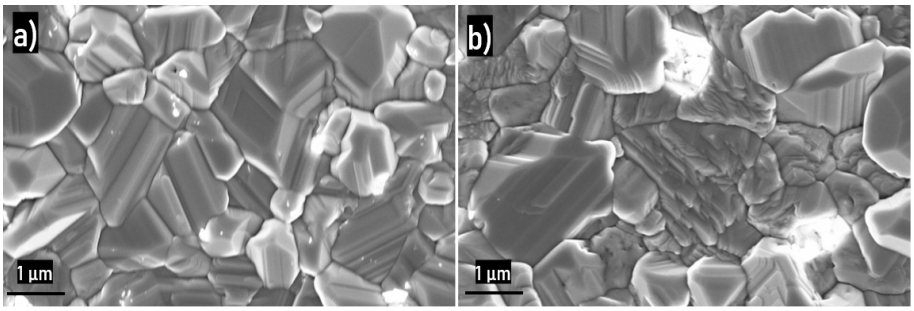

Figure 31: a) SEM image of kesterite CZTSSe surface after etching with 10 % w/w KCN for 30 min at RT. b) SEM image of kesterite CZTSSe surface after etching with 10 % w/w KCN for 60 min at RT.

Figure 31 shows that compared to the reference sample in Figure 30 the KCN does remove a significant amount of secondary phase selectively but contrarily, the HNO_3 etchant had no effect in removing any visible secondary phase as seen in Figure 32.

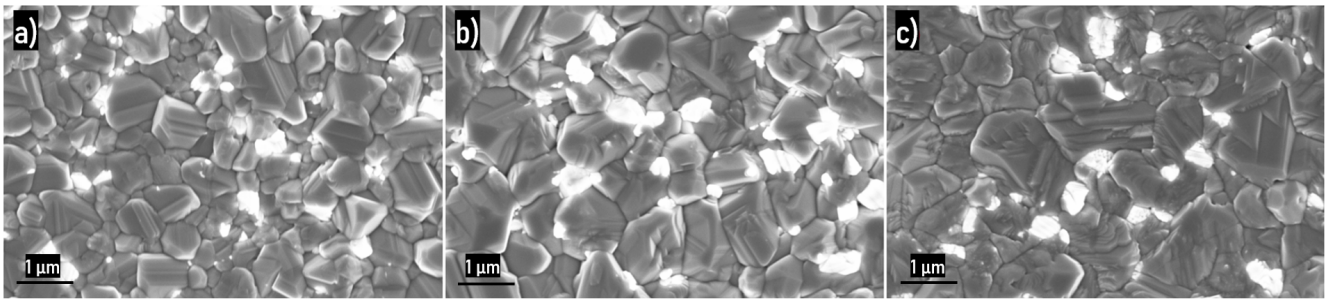

Figure 32: a) SEM image of kesterite CZTSSe surface after etching with 5 % v/v HNO_3 for 10 min at RT. b) SEM image of kesterite CZTSSe surface after etching with 5 % v/v HNO_3 for 5 min at RT. c) SEM image of kesterite CZTSSe surface after etching with 5 % v/v HNO_3 for 1.5 min at RT.

I-V and EQE Measurement

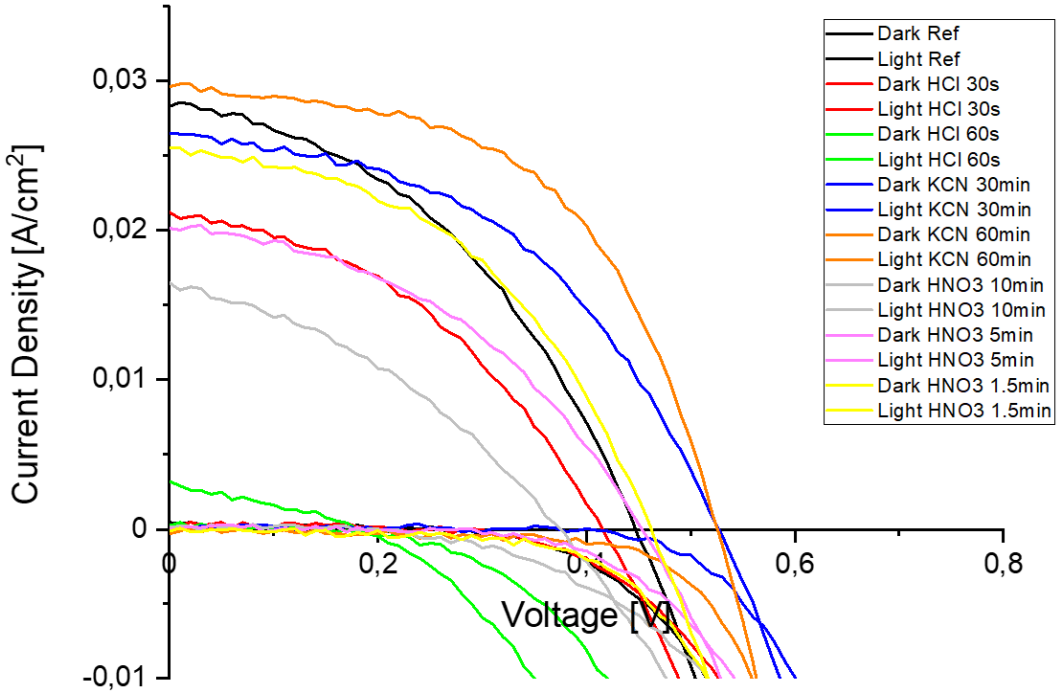

Figure 33: Current-Voltage measurement curves of PV devices with CZTSSe x=0.25, treated with different etchants and etching times.

Table 7: Resulting data of the I-V measurement curves of PV devices with CZTSSe x=0.25, treated with different etchants and etching times.

	Etchant	Cell Name	Efficiency, %	V_{OC}, V	J_{SC}, mA/cm^2	FF, %	P_{max}, W	R_{shunt}, Ω	R_{series}, Ω
1	Reference	D4	5.3	0.45	28.62	41.64	0.000374	48.208	6.275
2	5% HCl 30s	E2	3.6	0.42	21.21	41.58	0.000256	100.810	8.446
3	5% HCl 60s	C5	0.2	0.18	2.96	34.44	0.000013	81.778	36.682
4	10% KCN 30min	C3	6.4	0.53	26.59	46.17	0.000453	61.236	6.721
5	10% KCN 60min	E3	8.3	0.53	29.79	53.18	0.000582	56.549	4.072
6	5% HNO_3 10min	C2	2.2	0.37	16.46	36.16	0.000156	44.808	12.047
7	5% HNO_3 5min	D4	3.8	0.45	20.34	42.22	0.000272	28.207	8.948
8	5% HNO_3 1.5min	D4	5.3	0.46	25.40	45.74	0.000375	8.097	6.268

As it can be deduced from Figure 33 and Table 7 all samples which were etched with either HCl or HNO_3 dropped in PV efficiency as well as J_{SC}, Fill Factor and P_{max}. In contrary, the etching with KCN, both 30 min and 60 min improved in efficiency as well as J_{SC}, Fill Factor and P_{max}. An efficiency of 8.3 %, a J_{SC} of 29.79 mA/cm^2 and

a P_{max} of 0.000582 W were achieved.

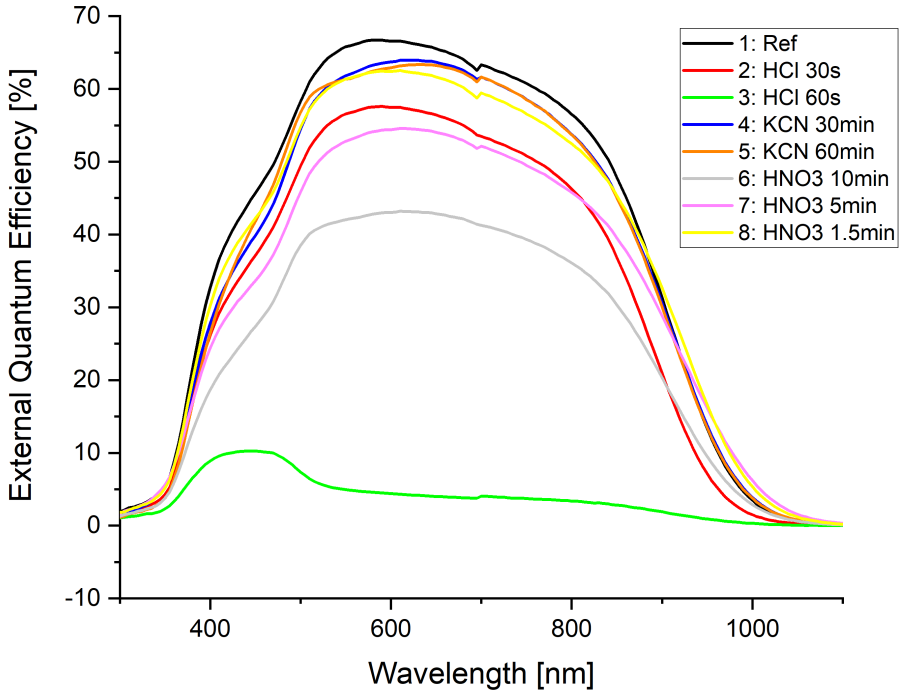

Figure 34: External Quantum Efficiency Measurement of the best cell of PV devices with CZTSSe x=0.25, treated with different etchants and etching times.

Even though the KCN etching on the kesterite CZTSSe absorber layer did improve the overall PV performance according to the I-V measurements in Table 7, the EQE measurements for the same cells resulted in no significant improvement compared to the reference cell as seen in Figure 34. Unlike I-V measurements, the measurement of the EQE does not consider other parameter of a PV device like the V_{OC} and the resistances of the device.However, the overall PV performance on all the PV device with absorber layers which were either chemically treated with HCl or with HNO_3 deteriorated. Samples which were treated with HCl performed worse compared to samples which were etched with HNO_3.

3.4.3 KCN Etching

Since KCN proved to be a suitable etchant for the selective removal of secondary phase of the CZT(S,Se) absorbers and therefore causing an improvement of their PV performance, further effects of different concentrations and etching time of KCN on the CZT(S,Se) absorbers were investigated.

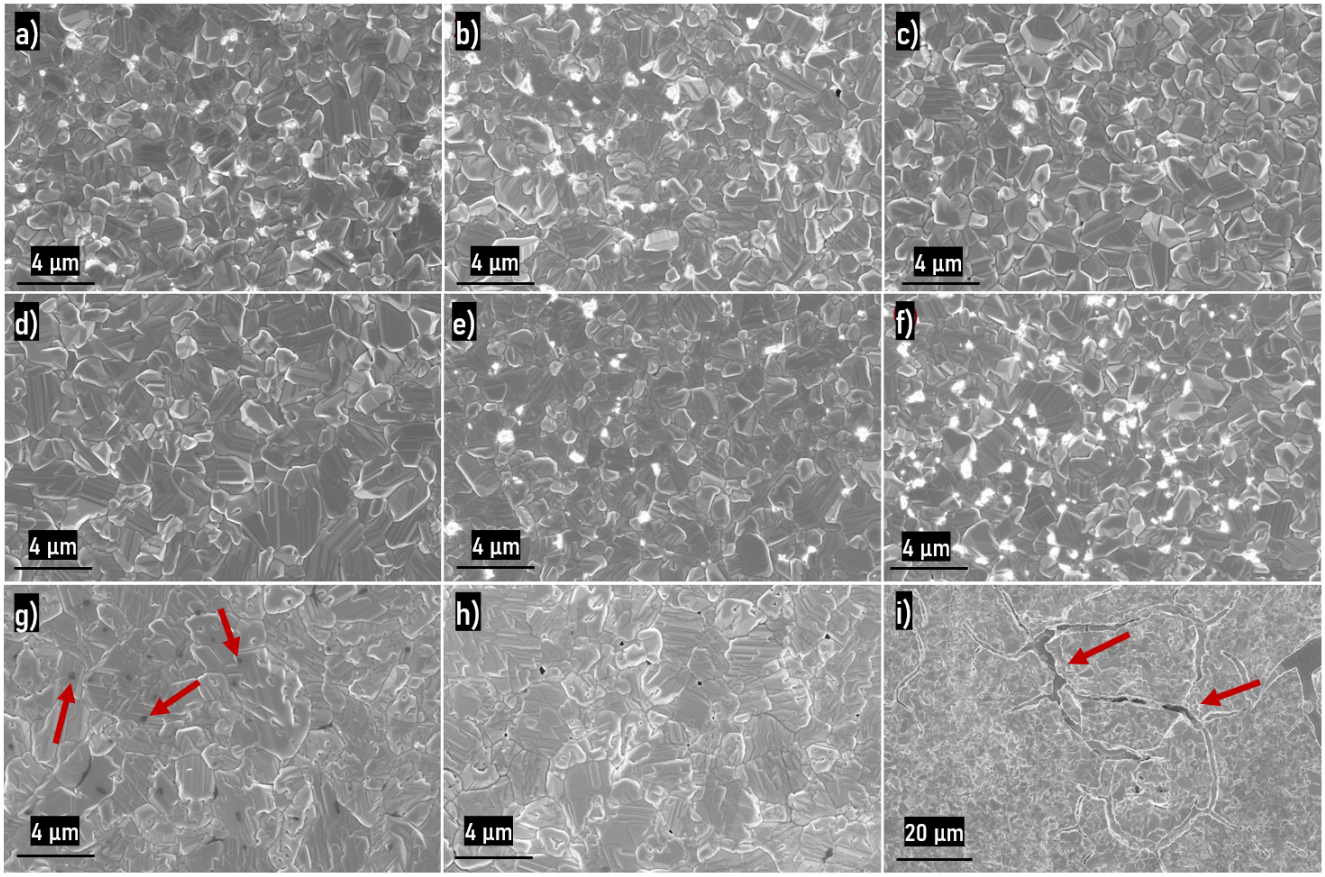

Figure 35: a) SEM image of kesterite CZTSSe surface as a reference. b) SEM image of kesterite CZTSSe surface after etching with 10 % w/w KCN for 60 min at RT. c) SEM image of kesterite CZTSSe surface after etching with 10 % w/w KCN for 90 min at RT. d) SEM image of kesterite CZTSSe surface after etching with 20 % w/w KCN for 30 min at RT. e) SEM image of kesterite CZTS surface after etching with 20 % w/w KCN for 60 min at RT. f) SEM image of kesterite CZTS surface after etching with 30 % w/w KCN for 15 min at RT. g) SEM image of kesterite CZTSSe surface after etching with 30 % w/w KCN for 30 min at RT. h) SEM image of kesterite CZTSSe surface after etching with 30% w/w KCN for 45min at RT. i) SEM image of kesterite CZTSSe surface after etching with 20 % w/w KCN for 45 min at RT.

The SEM images of the CZTSSe absorber layers which were etched show a partial removal of the visual superficial secondary phase. No visual difference could be noticed according to these images in regards to removing the secondary phase. However, the kesterite CZTSSe surface differs when the absorber was chemically etched with a concentration as high as 30% w/w, which can be seen especially in Figure 35 in g), where the surface shows

damages like darker spots when etched for 30 min and even cracks in i) when the absorber was etched for 45 min.

I-V and EQE Measurement

Table 8: Resulting data of the I-V measurements of PV devices with CZTSSe x=0.25, treated with different concentrations and etching times of KCN.

	Cell Name	Treatment	Efficiency, %	V_{OC}, V	J_{SC}, mA/cm^2	FF, %	P_{max} W	R_{shunt} , Ω	R_{series}, Ω
1	C3	Reference	5.0	0.48	25.20	41.01	0.000350	250.381	8.453
2	D3	10%KCN 60min	6.5	0.52	27.49	46.06	0.000457	39.366	6.273
3	F2	10%KCN 90min	5.7	0.49	27.09	42.99	0.000400	290.077	6.909
4	B2	20%KCN 30min	5.1	0.50	24.98	40.63	0.000356	29.373	8.649
5	B5	20%KCN 60min	6.9	0.56	26.15	47.28	0.000487	268.766	7.394
6	B4	30%KCN 15min	6.5	0.54	24.44	49.60	0.000456	277.164	6.424
7	-	30%KCN 30min	-	-	-	-	-	-	-
8	-	30%KCN 45min	-	-	-	-	-	-	-

Table 8 reveals that the PV performance of all PV devices in which the absorber layer was chemically etched with KCN improved their PV performance, except for the samples which were treated with 30 % w/w KCN for 30 min or longer which seemed to be destroyed in the etching process.
There is no significant improvement when the etching time and concentration exceed 60 min and 10 % w/w. It is worth mentioning that sample 4, which was treated with 20 % w/w KCN for 30 min showed the most even CZTSSe kesterite surface in Figure 35 in d), as no secondary phase was detected on the surface, but according to Table 8 this PV device performed the least efficient in this experiment, aside from the samples which were destroyed. The destruction of samples which were etched with 30 % w/w KCN for 30 min or longer is more predominantly illustrated in the EQE Figure 36, in which the very same sample which performed with less than an EQE of 50 %. Unfortunately, no EQE measurements could have been performed on any PV devices in which the absorber layers were etched with 30 % KCN for longer than 30 min. It is assumed that the etchant in such a high concentration as 30 % and an etching time of 30 min. and 45 min damages the kesterite CZTSSe surface. The damaging process of the 30 % KCN etchants already wears on for the sample which was etched with 30 % KCN for only 15 min. as is can be seen in its EQE curve.

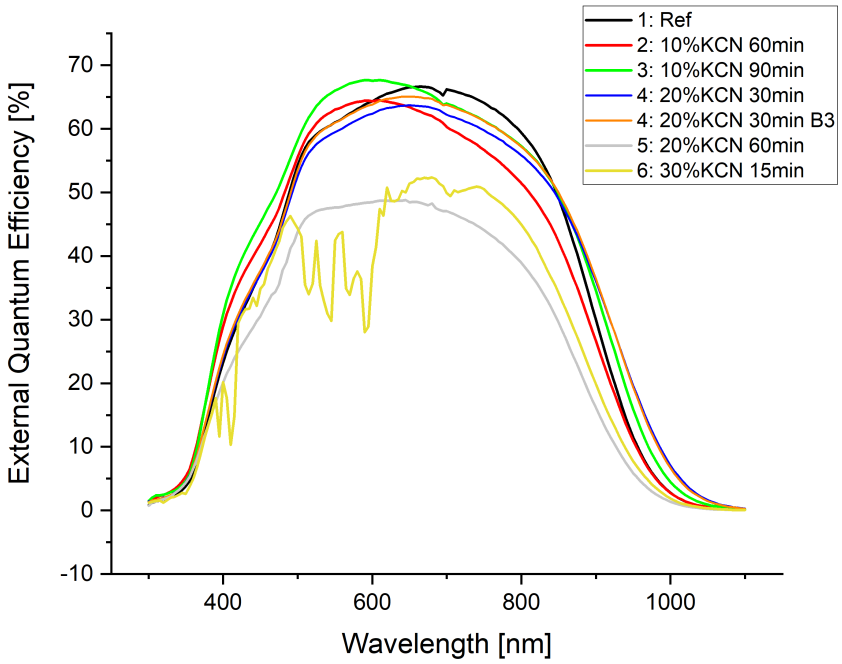

Figure 36: EQE measurement curves of PV devices with CZTSSe x=0.25, treated with different concentrations and etching times of KCN.

3.5 Thermal treatment

Three PV devices with a kesterite CZTSSe x=0.25 absorber, treated with 10 % w/w KCN for 60 min at room temperature where prepared. The best performing cells in the PV devices were determined using I-V measurements. After the IV-measurements, the samples were placed on a hot plate for at 150 °C, 175 °C or 200 °C for 15 min each. The very same cells were characterized using the solar simulator once again after the thermal treatments.

IV Curve Measurement

Table 9: Resulting data of the I-V measurement of PV devices with kesterite CZTSSe x=0.25 absorber, chemically etched with 10 % KCN for 60 min.

	Cell Name	Post-annealing Temperature	Efficiency, %	V_{OC}, V	J_{SC}, mA/cm^2	FF, %	P_{max}, W	R_{shunt}, Ω	R_{series}, Ω
1	D3	150°C	6.4	0.52	26.77	46.32	0.000449	332.665	6.783
2	B2	175°C	5.6	0.53	23.86	44.03	0.000392	205.191	9.007
3	E1	200°C	5.6	0.54	23.69	44.00	0.000394	310.406	8.650

Table 10: Resulting data of the I-V measurement of PV devices with kesterite CZTSSe x=0.25 absorber, chemically etched with 10% KCN for 60 min after thermal treatment for 15 min each.

	Cell Name	Post-annealing Temperature	Efficiency, %	V_{OC}, V	J_{SC}, mA/cm^2	FF, %	P_{max}, W	R_{shunt}, Ω	R_{series}, Ω
1	D3	150°C	5.8	0.53	25.85	42.47	0.000408	282.274	9.127
2	B2	175°C	1.7	0.56	12.51	24.38	0.000120	217.425	45.787
3	E1	200°C	3.8	0.57	20.22	33.34	0.000270	168.922	19.239

As presented in Table 9 and Table 10 the thermal treatment for every applied temperature decreased the performance of the PV devices. Figure 37 shows a CZTSSe PV device after a thermal treatment of 15 min at 175 °C. The thin film PV dematerialized in places where the Ag-paste was applied for contacting. This was observed in all samples which were post-annealed. It is to be assumed that the solvent which was used in this Ag-paste might dissolve the components of the CZTSSe PV device and therefore destroying it. The impact of the damage caused by the post-annealing on the hot plate correlates to the extent of the dematerialization of the sample beneath the Ag-paste. Therefore, the more material was destroyed, the lower the efficiency of the PV device. This can be seen as the sample, which was post-annealed at 175 °C exhibits more visual damage where it has been contacted using the Ag-paste than the other two samples.

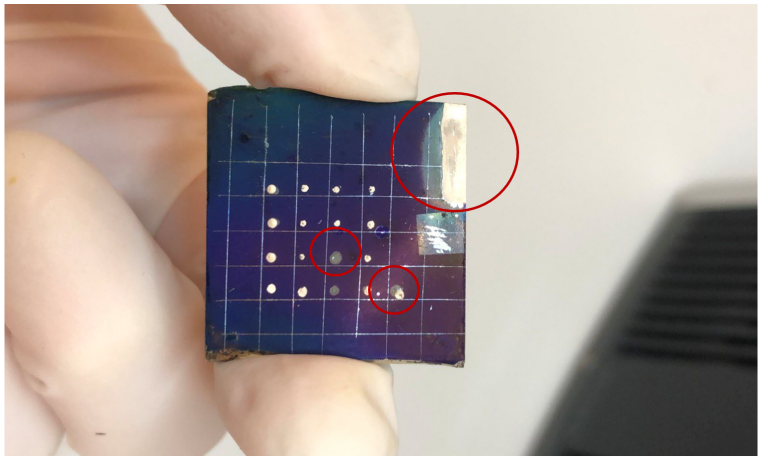

Figure 37: PV device with CZTSSe absorber, etched with 10% w/w KCN after thermal treatment at 175 °C. This problem was observed for every sample which was post-annealed at 150 °C, 175 °C and 200 °C.

4 Conclusion

In summary, CZTS/Se absorber layers were fabricated using a liquid precursor ink containing the earth abundant elements Copper, Zinc, Tin, Sulphur and subsequent annealing under co-evaporation with chalcogens Sulphur and/or Selenium. These as-annealed absorbers were characterized in regards to their thickness, crystallinity and surface morphology. Simultaneously, superficial secondary phases were identified using X-Ray diffraction and Raman spectroscopy.

Incorporated in photovoltaic devices, these absorbers were characterized using state-of-the-art photovoltaic characterization tools, including Current-Voltage measurements in a solar simulator and the measurement of the External Quantum efficiency.

Absorbers with different ratios of chalcogens Selenium and Sulphur were fabricated with which the Se/S ratio of x=0.25 proved to be the optimum for solar light absorption as this composition exhibited the best PV performance.

By examining the thickness of the as-annealed cross-section of a kesterite CZTSSe (x=0.25) absorber, the sufficient amount of spin coating cycles were determined to be at least 12 cycles to achieve a thickness of approximately 1.3 μm, which were incorporated in the successive absorber layer preparations.

The examination of the secondary phases in regards to their morphology and chemical composition allowed their systematic and selective removal using different chemical etching agents such as HCl, KCN and HNO_3. Both, HCl and KCN improved the surface morphology of the CZTSSe absorber by removing the secondary phases visually according to the images taken with Scanning Electron Microscopy. However, the photovoltaic characterization methods of Current-Voltage and External Quantum Efficiency measurements proved that HCl, despite low concentrations and etching times, decreased the performance of the PV device. Furthermore, the analysis with Raman spectroscopy lead to the suggestion that the etching with HCl even decreased the overall kesterite CZTSSe composition from x=0.25 to x=1. On the contrary, KCN demonstrated a selective removal of unwanted superficial secondary phases and an improvement of the PV performance was achieved when the etching parameters were 10% w/w in concentration and 60 min of etching time. Further etching parameters of the KCN etchants, such as 20% w/w and 30% w/w were investigated but no significant change could be noticed except for the fact that a concentration as high as 30% w/w put damage to the CZTSSe surface in a form of material cracks.

The thermal treatments seemed to face the challenge of the longevity of the PV device materials: the PV device diminished in spots where the Ag-paste was applied for contacting. This resulted in a poorer PV performance of the PV device compared to prior to the thermal treatments.

Howbeit, passing all of these optimization processes of the fabrication and characterization of kesterite CZTSSe PV devices, a photovoltaic device was prepared which accomplished to a solar efficiency of 8.3%, which is a significant improvement to its predecessor which performed with an solar efficiency of 4.7%.

References

[1] T. I. P. P. S. Programme, "Trends 2015 in photovoltaic applications," *Report No. IEA-PVPS T1-27*, 2015.

[2] A. Reinders, P. Verlinden, W. Van Sark, and A. Freundlich, *Photovoltaic Solar Energy: From Fundamentals to Applications*. John Wiley & Sons, 2017.

[3] P. W. Atkins and J. De Paula, *Physikalische Chemie*, pp. 343–344. John Wiley & Sons, 2002.

[4] R. Childs, *Atomic Physics*, pp. 135–140. Global Media, 2009.

[5] K. Mertens, *Photovoltaics: Fundamentals, Technology, and Practice*. John Wiley & Sons, 2018.

[6] H. K. Köthe, *Stromversorgung mit Solarzellen: Methoden und Anlagen für die Energieaufbereitung*, pp. 38–42. Franzis, 1988.

[7] M. Courel, A. Arce-Plaza, D. Oseguera-Galindo, and O. Vigil-Galan, "The path to improve kesterite solar cell efficiency," *General Chemistry*, vol. 4, no. 4, 2018.

[8] W. Wang, M. T. Winkler, O. Gunawan, T. Gokmen, T. K. Todorov, Y. Zhu, and D. B. Mitzi, "Device characteristics of CZTSSe thin-film solar cells with 12.6% efficiency," *Advanced Energy Materials*, vol. 4, no. 7, p. 1301465, 2014.

[9] S. Siebentritt, "Why are kesterite solar cells not 20% efficient?," *Thin Solid Films*, vol. 535, pp. 1–4, 2013.

[10] M. Ravindiran and C. Praveenkumar, "Status review and the future prospects of CZTS based solar cell-a novel approach on the device structure and material modeling for CZTS based photovoltaic device," *Renewable and Sustainable Energy Reviews*, vol. 94, pp. 317–329, 2018.

[11] C. Zeng, Y. Liang, L. Zeng, L. Zhang, J. Zhou, P. Huang, and R. Hong, "Effect of S/(S+ Se) ratio during the annealing process on the performance of $Cu_2ZnSn(S,Se)_4$ solar cells prepared by sputtering from a quaternary target," *Solar Energy Materials and Solar Cells*, vol. 203, p. 110167, 2019.

[12] S. Tripathi, S. Maurya, B. Kumar, and D. Dwivedi, "Comparative analysis of CZTS/CZTSe/CZTSSe absorber layer for solar cell applications," in *2020 International Conference on Electrical and Electronics Engineering (ICE3)*, pp. 588–591, IEEE, 2020.

[13] S. Abermann, "Non-vacuum processed next generation thin film photovoltaics: towards marketable efficiency and production of CZTS based solar cells," *Solar Energy*, vol. 94, pp. 37–70, 2013.

[14] H. Xie, Y. Sanchez, S. Lopez-Marino, M. Espíndola-Rodríguez, M. Neuschitzer, D. Sylla, A. Fairbrother, V. Izquierdo-Roca, A. Pérez-Rodríguez, and E. Saucedo, "Impact of Sn(S,Se) secondary phases in $Cu_2ZnSn(S,Se)_4$ solar cells: a chemical route for their selective removal and absorber surface passivation," *ACS Applied Materials & Interfaces*, vol. 6, no. 15, pp. 12744–12751, 2014.

[15] A. Fairbrother, E. García-Hemme, V. Izquierdo-Roca, X. Fontané, F. A. Pulgarín-Agudelo, O. Vigil-Galán, A. Pérez-Rodríguez, and E. Saucedo, "Development of a selective chemical etch to improve the conversion efficiency of Zn-rich Cu_2ZnSnS_4 solar cells," *Journal of the American Chemical Society*, vol. 134, no. 19, pp. 8018–8021, 2012.

[16] S. López-Marino, Y. Sánchez, M. Placidi, A. Fairbrother, M. Espindola-Rodríguez, X. Fontané, V. Izquierdo-Roca, J. López-García, L. Calvo-Barrio, A. Pérez-Rodríguez, *et al.*, "ZnSe etching of Zn-rich $Cu_2ZnSnSe_4$: an oxidation route for improved solar-cell efficiency," *Chemistry–A European Journal*, vol. 19, no. 44, pp. 14814–14822, 2013.

[17] S. Zhang, N. D. Pham, T. Tesfamichael, J. Bell, and H. Wang, "Thermal effect on CZTS solar cells in different process of ZnO/ITO window layer fabrication," *Sustainable Materials and Technologies*, vol. 18, p. e00078, 2018.

[18] U. Syafiq, N. Ataollahi, R. D. Maggio, and P. Scardi, "Solution-based synthesis and characterization of Cu_2ZnSnS_4 (CZTS) thin films," *Molecules*, vol. 24, no. 19, p. 3454, 2019.

[19] J. Ximello-Quiebras, G. Contreras-Puente, J. Aguilar-Hernandez, G. Santana-Rodriguez, and A. A.-C. Readigos, "Physical properties of chemical bath deposited CdS thin films," *Solar Energy Materials and Solar Cells*, vol. 82, no. 1-2, pp. 263–268, 2004.

[20] R. Mane and C. Lokhande, "Chemical deposition method for metal chalcogenide thin films," *Materials Chemistry and Physics*, vol. 65, no. 1, pp. 1–31, 2000.

[21] M. Kharrazi Olsson, *High-rate reactive magnetron sputter deposition and characterization of metal oxide films*. PhD thesis, Acta Universitatis Upsaliensis, 2000.

[22] H.-G. Wagemann, H. Eschrich, and H.-G. Wagemann, *Photovoltaik*, pp. 7–17. Springer, 2010.

[23] P. Hierrezuelo-Cardet, A. F. Palechor-Ocampo, J. Caram, F. Ventosinos, D. Pérez-del Rey, H. J. Bolink, and J. A. Schmidt, "External quantum efficiency measurements used to study the stability of differently deposited perovskite solar cells," *Journal of Applied Physics*, vol. 127, no. 23, p. 235501, 2020.

[24] R. A. Fleck and B. M. Humbel, *Biological Field Emission Scanning Electron Microscopy*. John Wiley & Sons, 2019.

[25] P. Larkin, *Infrared and Raman Spectroscopy: Principles and Spectral Interpretation*. Elsevier, 2017.

[26] M. Lee, *X-Ray Diffraction for Materials Research: from Fundamentals to Applications*. CRC Press, 2017.

[27] A. Redinger, K. Hönes, X. Fontané, V. Izquierdo-Roca, E. Saucedo, N. Valle, A. Pérez-Rodríguez, and S. Siebentritt, "Detection of a ZnSe secondary phase in coevaporated $Cu_2ZnSnSe_4$ thin films," *Applied Physics Letters*, vol. 98, no. 10, p. 101907, 2011.

[28] M. Altosaar, J. Raudoja, K. Timmo, M. Danilson, M. Grossberg, J. Krustok, and E. Mellikov, "$Cu_2Zn_{1-x}Cd_xSn(Se_{1-y}S_y)_4$ solid solutions as absorber materials for solar cells," *Physica Status Solidi (a)*, vol. 205, no. 1, pp. 167–170, 2008.

[29] M. Grossberg, J. Krustok, J. Raudoja, K. Timmo, M. Altosaar, and T. Raadik, "Photoluminescence and raman study of $Cu_2ZnSn(SexS1\text{-}x)_4$ monograins for photovoltaic applications," *Thin Solid Films*, vol. 519, no. 21, pp. 7403–7406, 2011.

[30] L. Grenet, P. Grondin, K. Coumert, N. Karst, F. Emieux, F. Roux, R. Fillon, G. Altamura, H. Fournier, P. Faucherand, *et al.*, "Experimental evidence of light soaking effect in Cd-free $Cu_2ZnSn(S,Se)_4$-based solar cells," *Thin Solid Films*, vol. 564, pp. 375–378, 2014.

[31] F. A. Jhuma, M. Z. Shaily, and M. J. Rashid, "Towards high-efficiency CZTS solar cell through buffer layer optimization," *Materials for Renewable and Sustainable Energy*, vol. 8, no. 1, pp. 1–7, 2019.

List of Figures

List of Tables